

Adaptive Markovian Spatiotemporal Transfer Learning in Multivariate Bayesian Modeling

Luca Presicce¹ and Sudipto Banerjee²

¹Department of Economics, Management and Statistics, Università degli studi Milano-Bicocca, Milano, Italy

²Department of Biostatistics, University of California, Los Angeles, California

Abstract

This manuscript develops computationally efficient online learning for multivariate spatiotemporal models. The method relies on matrix-variate Gaussian distributions, dynamic linear models, and Bayesian predictive stacking to efficiently share information across temporal data shards. The model facilitates effective information propagation over time while seamlessly integrating spatial components within a dynamic framework, building a Markovian dependence structure between datasets at successive time instants. This structure supports flexible, high-dimensional modeling of complex dependence patterns, as commonly found in spatiotemporal phenomena, where computational challenges arise rapidly with increasing dimensions. The proposed approach further manages exact inference through predictive stacking, enhancing accuracy and interoperability. Combining sequential and parallel processing of temporal shards, each unit passes assimilated information forward, then back-smoothed to improve posterior estimates, incorporating all available information. This framework advances the scalability and adaptability of spatiotemporal modeling, making it suitable for dynamic, multivariate, and data-rich environments.

Keywords— Bayesian inference; dynamic linear models, Bayesian predictive stacking; Spatiotemporal models; Markovian dependence.

1 Introduction

Spatiotemporal process models are a key statistical tool for analyzing data referenced by spatial locations and time points at which variables of interest have been measured (see, e.g., [Gelfand et al., 2010](#); [Cressie and Wikle, 2011](#); [Banerjee et al., 2025](#)). In particular, dynamic spatiotemporal models ((DSTM) [Stroud et al., 2001](#); [Gelfand et al., 2005](#); [Wikle and Hooten, 2010](#)), which build on a venerable literature on dynamic linear models (see the authoritative text by [West and Harrison, 1997](#)), offer probabilistic inference for the underlying stochastic processes ([Ali, 1979](#); [Cressie and Wikle, 2011](#); [Schmidt and Lopes, 2019](#)). These models can be recast as first-order affine discrete dynamical systems ([Sandefur, 1990](#); [Abdalla et al., 2020](#)), which provide an inferential framework

for modeling Markovian dependence structures. As state-space models, they encompass a variety of modeling frameworks adapted to a wide range of applications (e.g. [Nobre et al., 2005](#); [Gamerman et al., 2008](#); [Hefley et al., 2017](#); [Pherwani et al., 2024](#); [Idjigbèrou et al., 2025](#)).

Recent developments have increasingly focused on integrating ideas from statistical modeling, machine learning, physics, signal processing, and engineering. Probabilistic machine learning methods for physical systems, in particular, have relied on dynamic spatiotemporal modeling (see [Czaran and Bartha, 1992](#); [Chen et al., 2011](#), for examples in population dynamics and ecology). Developments in spatiotemporal analysis have attempted to integrate probabilistic machine learning with statistical inference based on Bayesian dynamic linear models (DLMS) (e.g. [Ivanovic and Pavone, 2019](#); [Zammit-Mangion and Wikle, 2020](#); [Banerjee et al., 2025](#)).

In order to employ AI-driven data analysis using dynamic spatiotemporal models for [Copernicus Data Space Ecosystem](#), we will (i) construct multivariate DLMS (see, e.g., [West and Harrison, 1997](#); [Gelfand et al., 2005](#); [Prado et al., 2021](#), for diverse modeling and inferential perspectives), and (ii) render spatial temporal hierarchical DLMS amenable to Bayesian transfer learning using amortized Bayesian inference ([Zammit-Mangion et al., 2025](#)). Toward this end, we devise an inferential framework based on closed-form distribution theory using matrix-variate Gaussian-Wishart families of conjugate DLMSS ([Quintana and West, 1987](#); [West and Harrison, 1997](#); [Landim and Gamerman, 2000](#); [Jiménez and Pereira, 2021](#); [Elkhouly and Ferreira, 2021](#); [Banerjee et al., 2025](#)). Our framework will scale probabilistic learning to massive volumes of data.

Amortized Bayesian inference involves training a deep learning network over a large number of simulated inputs from a specified model. Once trained, the network transfers the inference with the specified model to any new data set almost instantaneously ([Radev et al., 2020](#); [Zammit-Mangion et al., 2025](#)). However, training consumes substantial computational effort and exact posterior computations at the training phase may be preferred to expensive iterative algorithms such as Markov chain Monte Carlo (MCMC) or Integrated Nested Laplace Approximation (INLA).

Rather than using iterative algorithms, we exploit the analytical closed-form distribution theory available from the matrix-variate Gaussian-Wishart family. Here, we average over exact posterior distributions conditional on weakly identified hyperparameters that are, in any case, not consistently

estimable (Zhang, 2004; Tang et al., 2021). This approach is referred to as Bayesian predictive stacking ((BPS) Wolpert, 1992; Yao et al., 2018) and has recently been demonstrated by Zhang et al. (2025) as an effective inferential tool for Bayesian geostatistics.

We extend amortized Bayesian inference and predictive stacking to dynamic spatiotemporal models. Our proposed dynamic stacking method leverages the analytical tractability of DLM and alleviates computational costs for BPS. We adopt online transfer learning, where data are analyzed in a sequential stream of T time points, each corresponding to a temporal snapshot of a spatial random field. At each temporal data shard, we infer in parallel from closed-form posteriors for J models, each corresponding to fixed values of spatial kernel hyperparameters, and propagate inference to the next time shard using forward filtering. For each time shard, we assimilate inference across the J models using BPS and proceed with backward sampling from $t = T, T - 1, \dots, 1$ to complete the inference. A flow chart is supplied in Figure 1 comprising three steps within each temporal “cell”: (i) parallel computation of posterior distributions for each model specification; (ii) assimilate spatiotemporal inferences by stacking conjugate posteriors in closed form; and (iii) propagate information to the next step to deliver posterior-to-prior update.

The manuscript is organized as follows. Section 2 presents adaptive dynamic modeling and collects some of the necessary results on distribution theory that we will use. Section 3 provides details on the computational features of our inferential framework. Section 4 provides results from simulation studies and Section 5 analyzes the extracted multivariate data from the [Copernicus Data Space Ecosystem \(CDSE\)](#). The paper concludes with remarks and implications for future research in Section 6. Supplements to Sections 2, 3 and 4 are provided in Sections S1, S2 and S3, respectively. Section S4 provides an overview of the specific dataset we analyze. Finally, Section S5 collects additional figures that complement the core exposition.

2 Dynamic Spatiotemporal Multivariate Modeling

Spatiotemporal modeling focuses on transferring inference across time to efficiently learn from multivariate spatiotemporal processes. In this setting, our aim is to infer latent spatiotemporal fields,

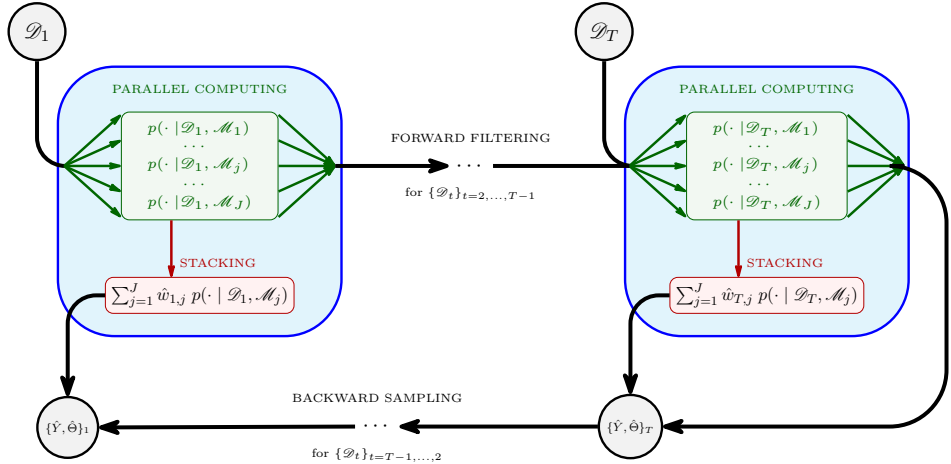


Figure 1: Data shards dynamics dependencies representation

which vary continuously in space and discretely in time. We automate inference propagation using a dynamic Bayesian predictive stacking framework.

2.1 Matrix-variate Dynamic linear models

Let $\{Y_t, t \in \mathcal{T}\}$ be a matrix-valued time series indexed by discrete time points in $\mathcal{T} = \{0, \pm 1, \pm 2, \pm 3, \dots\}$, where each $Y_t = \{Y_{i,j}^{(t)}\}$ is $n \times q$ with the (i, j) -th element $Y_{i,j}^{(t)}$ representing the recorded measurement of the variable $j \in \{1, \dots, q\}$ at spatial location $i \in \{1, \dots, n\}$. We let \mathcal{D}_t denote the data available to us up to time t , including the current observation Y_t , any covariates observed in t and all relevant past information \mathcal{D}_{t-1} with \mathcal{D}_0 denoting prior information without data.

A dynamic linear model decomposes each observation matrix Y_t into two time-dependent elements: the linear trend modeled as $F_t \Theta_t$ and the error Υ_t , which follows a matrix-variate normal distribution with row covariance V_t and column covariance Σ . The (latent) $(p \times q)$ matrix Θ_t , known as the “state” matrix at t , evolves smoothly over time, only depending on the previous state matrix Θ_{t-1} . Specifically, we formulate a matrix-variate DLM as

$$Y_t = F_t \Theta_t + \Upsilon_t, \quad \Upsilon_t \sim \text{MN}(0, V_t, \Sigma); \quad \Theta_t = G_t \Theta_{t-1} + \Xi_t, \quad \Xi_t \sim \text{MN}(0, W_t, \Sigma), \quad (1)$$

where $\Theta_0 \mid \Sigma \sim \text{MN}(m_0, C_0, \Sigma)$ represents the initial information on the state matrix, with m_0 and C_0 being the known $(p \times q)$ mean and $(p \times p)$ row covariance matrices, respectively. The prior information for the column covariance matrix is captured by $\Sigma \sim \text{IW}(\nu_0, \Psi_0)$ with the scalar

parameter ν_0 and the scale matrix Ψ_0 . Here, F_t is $n \times p$ with columns corresponding to explanatory predictors, G_t is $p \times p$ modeling the evolution of the state matrix, and W_t is $p \times p$ defining the dependence structure across the rows of Θ_t . Equations (1) are commonly called the “observation” and “state” equations. It is also assumed that Υ_t and Ξ_t are mutually independent and independent of $\{\Theta_0, \Sigma\}$. Additionally, given Θ_t , the variable Y_t is conditionally independent of past observations.

The Markovian structure in (1) facilitates efficient inference and prediction using the Kalman filter. Consequently, DLMs are particularly well-suited for online learning applications, enabling real-time updates to estimates as new data is observed. Sequential updating, forecasting, and retrospective smoothing naturally follow from familiar distribution theory (see, e.g., [West and Harrison, 1997](#); [Schmidt and Lopes, 2019](#), for necessary derivations).

The FFBS algorithm begins by “forward filtering” information through

$$\Theta_t \mid \mathcal{D}_{t-1}, \Sigma \sim \text{MN}(A_t, R_t, \Sigma) \quad (2)$$

and the one-step-ahead predictive distribution specified as

$$Y_t \mid \mathcal{D}_{t-1}, \Sigma \sim \text{MN}(q_t, Q_t, \Sigma), \quad (3)$$

where $A_t = G_t m_{t-1}$, $R_t = G_t C_{t-1} G_t^T + W_t$, $q_t = F_t A_t$, and $Q_t = F_t R_t F_t^T + V_t$. The filtered posterior distribution for $\{\Theta_t, \Sigma_t\}$ is specified by the following pair of distributions,

$$\Theta_t \mid \mathcal{D}_t, \Sigma \sim \text{MN}(m_t, C_t, \Sigma) \quad (4)$$

$$\Sigma \mid \mathcal{D}_t \sim \text{IW}(\nu_t, \Psi_t). \quad (5)$$

with $m_t = C_t [R_t^{-1} A_t + F_t^T V_t^{-1} Y_t]$, $C_t = [R_t^{-1} + F_t^T V_t^{-1} F_t]^{-1}$, $\nu_t = \nu_{t-1} + \frac{n}{2}$ and $\Psi_t = \Psi_{t-1} + \frac{1}{2}(Y_t - q_t)^T Q_t^{-1} (Y_t - q_t)$. Once the filtered posterior distribution $p(\Theta_t \mid Y_{1:t}, \Sigma)$ is recovered for all $t = 1, \dots, T$, the “backward sampling” algorithm is applied to smooth and refine state matrix estimates using both past and future knowledge. The smoothed posterior distributions are then

computed backward:

$$\Theta_t \mid \Theta_{t+1}, \mathcal{D}_T, \Sigma \sim \text{MN}(h_t, H_t, \Sigma) \quad (6)$$

where $h_t = H_t[C_t^{-1}m_t + G_{t+1}^T W_{t+1}^{-1} \Theta_{t+1}]$, and $H_t = [C_t^{-1} + G_{t+1}^T W_{t+1}^{-1} G_{t+1}]^{-1}$. Posterior inference for DLMs just involves two steps: forward filtering information using Equations from (2) to Equation (5), and smoothed future information backward by in (6).

Bayesian predictive forecasts are also straightforward here. Given a prediction horizon k , the joint predictive distribution for the state and observation matrices Θ_{T+k}, Y_{T+k} is

$$\begin{bmatrix} \Theta_{T+k} \\ Y_{T+k} \end{bmatrix} \mid Y_{1:T}, \Sigma \sim \text{MN} \left(\begin{bmatrix} A_T(k) \\ q_T(k) \end{bmatrix}, \underbrace{\begin{bmatrix} R_T(k) & F_{T+k} R_T(k) \\ R_T(k) F_{T+k}^T & Q_T(k) \end{bmatrix}}_{A^*(k) \quad R^*(k)}, \Sigma \right), \quad (7)$$

where $A_T(k) = G_{T+k} A_T(k-1)$, $R_T(k) = G_{T+k} R_T(k-1) G_{T+k}^T + W_{T+k}$, $q_T(k) = F_{T+k} A_T(k)$, and $Q_T(k) = F_{T+k} R_T(k) F_{T+k}^T + V_{T+k}$, with $A_T(0) = m_T$, $R_T(0) = C_T$. Parameters are updated recursively and are calculated for previous $k-1$ steps to obtain k -step-up forecasts.

We introduce spatial dependence in (1) using an augmented linear model (see, e.g., [Banerjee, 2020](#), for a univariate spatial example) that absorbs the spatial effects. Writing $F_t = [X_t : \mathbb{I}_n]$ as $n \times (p+n)$ and $\Theta_t = [B_t^T : \Omega_t^T]^T$ as $(p+n) \times q$, where p is the number of available predictors in X_t , B_t is the matrix $(p \times q)$ of dynamic regression coefficients, and Ω_t is the latent matrix $(n \times q)$ of spatial process realizations in n locations and q variables. We further assume $B_t \perp\!\!\!\perp \Omega_t \forall t \in \mathcal{T}$, leading to $G_t = \begin{bmatrix} \mathbb{I}_p & 0_{p \times n} \\ 0_{n \times p} & \mathbb{I}_n \end{bmatrix}$. This yields

$$\begin{aligned} Y_t &= \underbrace{\begin{bmatrix} X_t & \mathbb{I}_n \end{bmatrix}}_{F_t} \underbrace{\begin{bmatrix} B_t \\ \Omega_t \end{bmatrix}}_{\Theta_t} + \Upsilon_t, \quad \Upsilon_t \sim \text{MN}(0, V_t(\alpha), \Sigma); \\ \underbrace{\begin{bmatrix} B_t \\ \Omega_t \end{bmatrix}}_{\Theta_t} &= \underbrace{\begin{bmatrix} \mathbb{I}_p & 0_{p \times n} \\ 0_{n \times p} & \mathbb{I}_n \end{bmatrix}}_{G_t} \underbrace{\begin{bmatrix} B_{t-1} \\ \Omega_{t-1} \end{bmatrix}}_{\Theta_{t-1}} + \Xi_t, \quad \Xi_t \sim \text{MN}(0, W_t(\phi), \Sigma), \end{aligned} \quad (8)$$

where $V_t(\alpha) = (\frac{1-\alpha}{\alpha})\mathbb{I}_n$, $W_t(\phi) = \begin{bmatrix} W_t^B & 0_{p \times n} \\ 0_{n \times p} & R_t(\mathcal{S}, \mathcal{S}; \phi) \end{bmatrix}$, W_t^B is a generic $p \times p$ row-covariance matrix for dynamic coefficients and $R_t(\mathcal{S}, \mathcal{S}; \phi)$ is an $n \times n$ spatial correlation matrix using locations enumerated in the set $\mathcal{S} = \{s_1, \dots, s_n\}$. The (i, j) -th element of $R_t(\mathcal{S}, \mathcal{S}; \phi)$ is the value of a spatial correlation function (e.g., an exponential or Matérn with parameters ϕ) evaluated at locations s_i and s_j . The specification for $V_t(\alpha)$ introduces a discontinuity accounting for micro-scale measurement error (“nugget”). In doing so, we introduce a parameter α that captures the proportion of total variability expressed by the spatial component. The model in (8) produces the same structure as a DLM. Hence, the conditional posterior distribution of $\{\Theta_t, \Sigma\}$, given fixed values of $\{\alpha, \phi\}$, is available to us in closed form from (4) and (5).

In addition to temporal forecasting, we consider spatial interpolation. The target involves interpolating the latent spatial process for unobserved points. Here, we consider space as continuous and time as discrete. Thus, we are looking for spatial interpolation at each time point. To be precise, for $t \in \mathcal{T}$, we let \tilde{Y}_t denote the matrix of unknown values of the outcome on a set of m unobserved spatial locations enumerated as $\mathcal{U} = \{u_1, \dots, u_m\}$. We assume that \tilde{F}_t and $\tilde{\Omega}_t$ are the realizations of the latent spatial process at unobserved locations. Thus, we seek the posterior predictive distribution defined as

$$p(\tilde{Y}_t, \tilde{\Omega}_t \mid \mathcal{D}_t) = \int \left[\int p(\tilde{Y}_t, \tilde{\Omega}_t \mid \mathcal{D}_t, \Theta_t, \Sigma) p(\Theta_t \mid \mathcal{D}_t, \Sigma) d\Theta_t \right] p(\Sigma \mid \mathcal{D}_t) d\Sigma. \quad (9)$$

For the model in Equation (8), the integral in (9) can be computed analytically (using similar arguments used in [Presicce and Banerjee, 2024](#), Supplement 1.1). In particular, we pursue full predictive inference on outcomes and spatial latent processes with the following matrix-variate Student's t posterior predictive distribution

$$p(\tilde{Y}_t, \tilde{\Omega}_t \mid \mathcal{D}_t) = T_{2m, q}(\nu_t, \mu_t, E_t, \Psi_t, \nu_t), \quad (10)$$

where $\mu_t = \chi_t m_t$, $E_t = \chi_t C_t \chi_t^T + N_t$, with $\chi_t = \begin{bmatrix} \tilde{X}_t & \tilde{M}_t \\ 0 & \tilde{M}_t \end{bmatrix}$, $N_t = \begin{bmatrix} \tilde{V}_t(\alpha) + \tilde{W}_t(\phi) & \tilde{W}_t(\phi) \\ \tilde{W}_t(\phi) & \tilde{W}_t(\phi) \end{bmatrix}$. Here, $\tilde{V}_t(\alpha) = (\frac{1-\alpha}{\alpha})\mathbb{I}_m$ is the row-covariance matrix for \tilde{Y}_t , while $\tilde{M}_t = \mathcal{R}_t(\mathcal{U}, \mathcal{S}; \phi) \mathcal{R}_t^{-1}(\mathcal{S}, \mathcal{S}; \phi)$ and

$\tilde{W}_t(\phi) = \mathcal{R}_t(\mathcal{U}, \mathcal{U}; \phi) - \mathcal{R}_t(\mathcal{U}, \mathcal{S}; \phi) \mathcal{R}_t^{-1}(\mathcal{S}, \mathcal{S}; \phi) \mathcal{R}_t(\mathcal{S}, \mathcal{U}; \phi)$ are the mean and row-covariance matrices, respectively, specifying $p(\Omega_t \mid \mathcal{D}_t)$.

2.2 Parallel adaptive spatiotemporal propagation

Section 2.1 augmented standard matrix-variate dynamic linear models to incorporate spatiotemporal processes. Similar approaches have been investigated for complex data analysis (see e.g. Jiménez and Pereira, 2021). Our contribution here relies on a dynamic adjustment of Bayesian predictive stacking (BPS) that will allow the FFBS algorithm to exploit conjugate distribution theory and scale inference to large spatiotemporal datasets without resorting to MCMC algorithms.

BPS (as formulated in Yao et al., 2018) is a widely applicable model averaging method that has been shown to be effective for spatial data analysis (see Zhang et al., 2025; Presicce and Banerjee, 2024). Recently, Pan et al. (2025) developed BPS for hierarchical stochastic process models using spatiotemporal covariance kernels; however, their method does not scale to the massive size of our Copernicus dataset. Bayesian DLMSS treat time as discrete epochs, which allows the FFBS algorithm to scale to large temporal datasets. We consider BPS an effective transfer learning tool that can analyze massive volumes of spatiotemporal data. We achieve this by implementing a “dynamic” variation for predictive stacking that takes advantage of the predictive structure of DLMs.

A key advantage of our adaptation of BPS is that it will retain the full conjugacy of the model in Equation (8). Note that if $\{\alpha, \phi\}$ is fixed, then the model in (8) yields posterior distributions in closed form. Sampling from this posterior distribution is exact using the FFBS algorithm, and we do not require iterative algorithms such as MCMC approaches. Therefore, we fix $\{\alpha, \phi\}$ for a set of values and treat each value, $\alpha_{(j)}, \phi_{(j)}$, for $j = 1, \dots, J$ to correspond to a model \mathcal{M}_j . We obtain inference by stacking (Breiman, 1996).

BPS attempts to find the optimal distribution in the convex hull $\mathcal{C} = \{\sum_{j=1}^J w_j p(\cdot \mid \mathcal{M}_j) : \sum_{j=1}^J w_j = 1, w_j \geq 0\}$ of individual posterior distributions by maximizing a proper scoring rule (Gneiting and Raftery, 2007; Yao et al., 2018). Choices for a specific scoring rule include the true predictive distribution, which, however, is unknown and is computed using a leave-one-out estimate (see Yao et al., 2018, Section 3.1). This has been shown to be effective in Bayesian geostatistics

(Zhang et al., 2025), but may not be ideal for capturing temporal dependencies. Hence, we introduce leave-future-out (LFO) based on gleanings from Paul-Christian Bürkner and Vehtari (2020); Vehtari et al. (2016, 2017) to account for temporal dependencies in our data. LFO cross-validation and similar approaches that account for dependence in validation problems have also been investigated in Ruiz Maraggi et al. (2021); Cooper et al. (2023); Kennedy et al. (2024).

We adopt the one-step-ahead predictive distribution as our scoring function to assess the model's predictive performance in time-dependent contexts. In S1.1 we provide further details on deriving the optimization problem for dynamic predictive stacking. Dynamic stacking weights at time τ are then computed by solving this optimization problem

$$\hat{w}_i^{(\tau)} = \operatorname{argmax}_{w_i^{(\tau)} \in \mathcal{S}_1^J} \frac{1}{\tau-1} \sum_{t=1}^{\tau-1} \log \sum_{j=1}^J w_{i,j}^{(\tau)} \underbrace{p(Y_{t+1,i} \mid \mathcal{D}_t, \mathcal{M}_j)}_{T_{1,q}(Y_{t+1,i} \mid \nu_t^{(j)}, q_{t+1,i}^{(j)}, Q_{t+1,i}^{(j)}, \Psi_t^{(j)})}. \quad (11)$$

where $Y_{t,i}$ is the i -th row of Y_t , $p(Y_{t,i} \mid \mathcal{D}_{t-1}, \mathcal{M}_j)$ corresponds to the marginalization of the one-step ahead predictive distribution in (3) based on \mathcal{M}_j fixed parameters, and \mathcal{S}_1^J is the simplex of dimension J . The marginal predictive density $p(Y_{t,i} \mid \mathcal{D}_{t-1}, \mathcal{M}_j)$, is available in closed form as a matrix-variate t distribution $T_{1,q}(Y_{t+1,i} \mid \nu_t^{(j)}, q_{t+1,i}^{(j)}, Q_{t+1,i}^{(j)}, \Psi_t^{(j)})$, where $q_{t+1,i}^{(j)} = F_{t+1,i} A_{t+1}^{(j)}$, $Q_{t+1,i} = F_{t+1,i} R_{t+1}^{(j)} F_{t+1,i} + V_{t+1}(\alpha_j)$; $A_{t+1}^{(j)} = G_{t+1} m_t^{(j)}$, and $R_{t+1}^{(j)} = G_{t+1} C_t^{(j)} G_t^T + W_t(\phi_j)$. For each step t , the parameters $\{\nu_t^{(j)}, C_t^{(j)}, \Psi_t^{(j)}, \nu_{t-1}^{(j)}\}$ are inherited from the previous step $t-1$ for each model \mathcal{M}_j .

In addition, at each time instant t , the one-step ahead predictive distributions are computed by default within THE FFBS procedure (see (3)). These distributions exactly match the one-step ahead predictive distribution required by LFO cross-validation.

It is worth remarking that we compute stacking weights for each location i in Algorithm 1, which corresponds to a single time series, and for each time $t = 2, \dots, T$. This comes primarily from the dynamic natural stacking weights in (11). We compare predictive performance across time instants and not across observations as standard Bayesian predictive stacking does. This originates from the difference between leave-one-out cross-validation and leave-future-out cross-validation (schematized in Figure 2). However, even if it is theoretically possible to design this way, a simultaneous evaluation

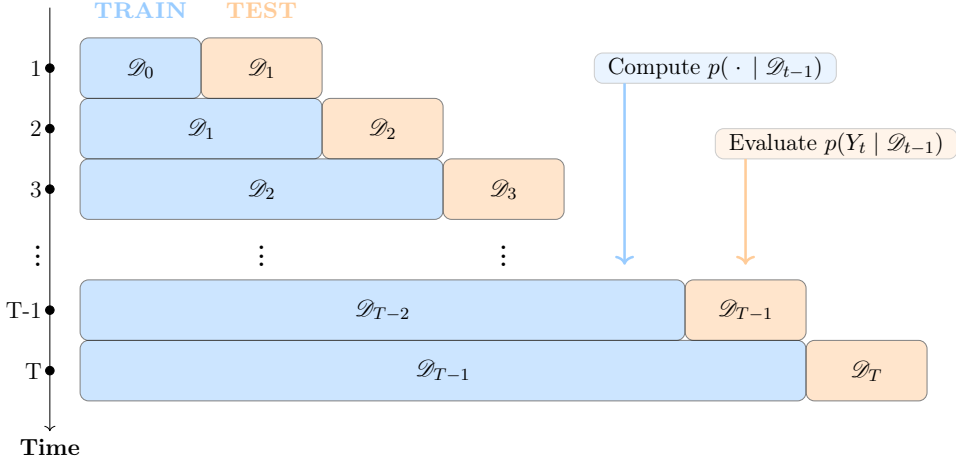


Figure 2: Leave-future-out cross-validation

across time and locations is infeasible. As the number of points increases, the density lies in a higher-dimensional space, where the notion of a point rapidly loses sense, and its probability goes to zero even faster. Then, as the number of locations grows, the evaluation of the predictive density for the whole matrix Y_t results in numerical instabilities. Nevertheless, individual evaluations allow us to reach a finer granularity of stacking weights and possibly provide individual temporal inferences for each location. Individual stacking weights are useful instruments to extract insight into model competition in several areas of interest, as shown in Section 4 using simulated data.

However, performing posterior inference on the parameters using Algorithm 3, required a unique set of stacking weights. Moreover, posterior inference on parameters should not depend on single locations, even though it is possible to do so. Let us aware the reader aware that performing individual posterior inferences may turn into an excessively demanding computational burden, along with the use of global weights for this scope. Parallel computing may be helpful in this matter but requires high computational resources to lighten individual inferences over n locations, especially in big- n settings.

To retain computational admissibility over the locations, we propose two approaches to achieve stacking weights. We may opt for the average weights across all locations, i.e.

$$\{\hat{w}_1^{(\tau)}, \dots, \hat{w}_J^{(\tau)}\} = \hat{w}_G^{(\tau)} = \frac{1}{n} \sum_{i=1}^n \hat{w}_i^{(\tau)} = \left\{ \frac{1}{n} \sum_{i=1}^n \hat{w}_{i,1}^{(\tau)}, \dots, \frac{1}{n} \sum_{i=1}^n \hat{w}_{i,J}^{(\tau)} \right\},$$

referring to them as “global” weights and indexed with the subscript G . Alternatively, we may consider the consensus across all locations. Let the number of observations for which model j has the maximum weight be denoted by $c_j^{(\tau)} = \left| \{i : j_i^{(\tau)} = j\} \right|$ with $j_i^{(\tau)} = \arg \max_{1 \leq j \leq J} \hat{w}_{i,j}^{(\tau)}$. We then define the consensus weight vector by normalizing these counts:

$$\{\hat{w}_{C,1}^{(\tau)}, \dots, \hat{w}_{C,J}^{(\tau)}\} = \hat{w}_C^{(\tau)} = \left\{ \frac{c_1^{(\tau)}}{n}, \dots, \frac{c_J^{(\tau)}}{n} \right\}.$$

We refer to these as “consensus” weights and index them with the subscript C . Both these solutions provide a set of weights that is still a regular vector of probabilities. In Section S1.2, guaranties that both strategies provide probability vectors are given. We further provide an empirical investigation of the impact of this choice in Section 4.

After we have obtained the set of dynamic weights at time τ and $\hat{w}^{(\tau)}$ based on the preferred aggregation strategy, posterior inference follows straightforwardly using the stacked posterior distribution,

$$\hat{p}(\cdot \mid \mathcal{D}_\tau) = \sum_{j=1}^J \hat{w}_j^{(\tau)} p(\cdot \mid \mathcal{D}_\tau, \mathcal{M}_j), \quad (12)$$

where \cdot denotes the inferential object of interest (e.g., regression parameters; latent process; predictive values at a location or time). We sample from (12) by first sampling one of the J posteriors, $p(\cdot \mid \mathcal{D}_\tau, \mathcal{M}_j)$ with probability \hat{w}_j , and then sampling \cdot from the drawn posterior.

The computational procedure needed to compute the individual stacking weights within each time shard is depicted in Algorithm (1). We take advantage of parallel computing over the competitive model evaluation, as the number J of competitive models in most applications allows for a light implementation even in modest computational environments.

A substantial problem arises when borrowing temporal posterior-to-prior information throughout FFBS using the content presented so far. Indeed, predictive stacking results in posterior distributions defined as finite mixtures, see Equation (12). This could break the FFBS machinery, i.e., its conjugacy across previous instant posteriors acting as priors for the next one. a solution to the mutual information must be found. Intuitively, a solution relies on assimilating a parallel learning path for each model. Thus, the stacked distribution retains reliability for inference in each generic dataset

Algorithm 1 Computing individual DYNBPS weights at time τ

Require: Data \mathcal{D}_τ , one-step-ahead predictive and filtered posterior parameters $\left\{q_\tau^{(j)}, Q_\tau^{(j)}, \nu_{\tau-1}^{(j)}, \Psi_{\tau-1}^{(j)}\right\}_{j=1}^J$, one-step-ahead predictive density evaluations $\left\{pd_{i,j}^{(t)}\right\}_{t=1}^{\tau-1}$

Ensure: Individual stacking weights at time τ

- 1: **for** $i = 1, \dots, n$ **do**
- 2: *# Evaluate one-step-ahead posterior predictive density for Y_τ*
- 3: $pd_{i,j}^{(\tau)} \leftarrow dT_{1,q}(Y_{\tau,i} \mid \nu_{\tau-1}^{(j)}, q_{\tau,i}^{(j)}, Q_{\tau,i}^{(j)}, \Psi_{\tau-1}^{(j)})$
- 4: *# Obtain DYNBPS weights solving the convex optimization problem*
- 5: $\hat{w}_i^{(\tau)} \leftarrow \underset{w_i^{(\tau)} \in \mathcal{S}_1^J}{\operatorname{argmax}} \frac{1}{\tau-1} \sum_{t=1}^{\tau-1} \log \sum_{j=1}^J w_{i,j}^{(\tau)} pd_{i,j}^{(t+1)}$
- 6: **end for**
- 7: **return** $\left\{\hat{w}_i^{(\tau)} = \left\{\hat{w}_{i,1}^{(\tau)}, \dots, \hat{w}_{i,J}^{(\tau)}\right\}\right\}_{i=1}^n$

\mathcal{D}_τ , but information to the incoming dataset $\mathcal{D}_{\tau+1}$ only passes across J parallel learning paths. Then, posterior-to-prior distribution retains the conjugacy of FFBS algorithm, as we do not use stacked posterior $\hat{p}(\cdot \mid \mathcal{D}_\tau)$ but conditional posterior instead, i.e. $p(\cdot \mid \mathcal{D}_\tau, \mathcal{M}_j)$ for $j = 1, \dots, J$. Hence, these computational adaptations allow us to preserve the conjugacy in the FFBS algorithm while borrowing information between time instants.

Thus, we found a solution that allows us to average out nuisance spatial parameters, and this was obtained by adapting instruments from BPS into a dynamical environment. It is worth specifying that the conditional posterior distributions do not affect the inference within each data shard at a specific time instant. In practice, conditional posterior distributions, are only used to allow the information propagation across time, but inferences are pursued by stacked posterior. This permits us to take advantage of the finite mixture formulation of stacked posterior gained from BPS, making it possible to fit more complex distributions, for prediction and uncertainty quantification. Figure 1 provides a graphical representation of the entire procedure within each “cell”.

3 Computational details

Standard Bayesian inference for DYNAMICS proceed with the well-known forward filter and backward sampling, if possible. Indeed, conjugacy is generally not available for all parameters. In spatial and spatiotemporal settings, spatial range parameters introduce complications. Circumnavigating this problem requires the implementation of simulation-based approaches, e.g. MCMC, to perform sampling from posterior distributions, making conjugacy only exploitable as full conditional anal-

Algorithm 2 DYNBPS - parallel forward filter

Require: Data $\mathcal{D}_{1:T}$, observation and state transition matrices $F_{1:T}, G_{1:T}$, starting stacking weights $\hat{w}^{(0)}$, hyperparameters $\left\{m_0^{(j)}, C_0^{(j)}, \Psi_0^{(j)}, \nu_0^{(j)}, \alpha^{(j)}, \phi^{(j)}\right\}_{j=1}^J$

Ensure: Filtering distribution parameters, stacking weights at time $t = 0, \dots, T$

- 1: **function:** PARALLELFORWFILT $\left(\mathcal{D}_{1:T}, F_{1:T}, G_{1:T}, \hat{w}^{(0)}, \left\{m_0^{(j)}, C_0^{(j)}, \Psi_0^{(j)}, \nu_0^{(j)}, \alpha^{(j)}, \phi^{(j)}\right\}_{j=1}^J\right)$
- 2: **for** $t = 1, \dots, T$ **do**
- 3: **for** $j = 1, \dots, J$ **do Parallel**
- 4: *# Compute observation and state row-covariance matrices*
- 5: $V_t^{(j)} \leftarrow \left(\frac{1-\alpha^{(j)}}{\alpha^{(j)}}\right) \mathbb{I}_n, W_t^{(j)} \leftarrow \begin{bmatrix} \mathbb{I}_p & 0_{p \times n} \\ 0_{n \times p} & \mathcal{R}_t(\mathcal{S}, \mathcal{S}; \phi^{(j)}) \end{bmatrix}$
- 6: *# Compute filtered prior parameters*
- 7: $A_t^{(j)} \leftarrow G_t m_{t-1}^{(j)}, R_t^{(j)} \leftarrow G_t C_{t-1}^{(j)} G_t^T + W_t^{(j)}$
- 8: *# Compute one-step ahead predictive parameters*
- 9: $q_t^{(j)} \leftarrow F_t A_t^{(j)}, Q_t \leftarrow F_t R_t^{(j)} F_t^T + V_t^{(j)}$
- 10: *# Compute state matrix filtered posterior parameters*
- 11: $m_t^{(j)} \leftarrow C_t^{(j)} \left[(R_t^{(j)})^{-1} A_t^{(j)} + F_t^T (V_t^{(j)})^{-1} Y_t \right], C_t^{(j)} \leftarrow \left[(R_t^{(j)})^{-1} + F_t^T (V_t^{(j)})^{-1} F_t \right]^{-1}$
- 12: *# Compute column-covariance matrix filtered posterior parameters*
- 13: $\nu_t^{(j)} \leftarrow \nu_{t-1}^{(j)} + \frac{n}{2}, \Psi_t^{(j)} \leftarrow \Psi_{t-1}^{(j)} + \frac{1}{2} (Y_t - q_t^{(j)})^T (Q_t^{(j)})^{-1} (Y_t - q_t^{(j)})$
- 14: **end Parallel for**
- 15: *# Obtain individual weights using Algorithm 1 and compute global weights*
- 16: $\left\{\hat{w}_i^{(t)} = \left\{\hat{w}_{i,1}^{(t)}, \dots, \hat{w}_{i,J}^{(t)}\right\}\right\}_{i=1}^n, \hat{w}^{(t)} \leftarrow \frac{1}{n} \sum_{i=1}^n \hat{w}_i^{(t)} = \left\{\frac{1}{n} \sum_{i=1}^n \hat{w}_{i,1}^{(t)}, \dots, \frac{1}{n} \sum_{i=1}^n \hat{w}_{i,J}^{(t)}\right\}$
- 17: **end for**
- 18: **return** $\left\{\hat{w}^{(t)}, \left\{m_t^{(j)}, C_t^{(j)}, \Psi_t^{(j)}, \nu_t^{(j)}\right\}_{j=1}^J\right\}_{t=0}^T$
- 19: **end function**

ysis in Metropolis-within-Gibbs frameworks. In this work, we aim to completely avoid simulation or iterative-based methodologies, seeking a full conjugate analysis for DSTMss. Vanilla implementations of Bayesian predictive stacking, let alone the advantages, also introduce drawbacks. The BPS posterior distributions are finite mixtures; this breaks down posterior-to-prior updating, which allows borrowing of information through time instants in the forward filter and backward sampling algorithm. The same happens for more sophisticated BPS based modeling approaches (e.g., [Presicce and Banerjee, 2024](#)). A feasible solution to retain THE algorithm structure of the FFBS algorithm should include temporal dynamics within the Bayesian predictive stacking while preserving conjugate posterior-to-prior updates. In section 2, we then propose a dynamic strategy based on Bayesian predictive stacking of predictive distributions. Algorithm 1 shows its implementation.

We now present the computational adjustment to the algorithms characterizing the FFBS procedure ([Carter and Kohn, 1994](#)). This series of algorithms replaces the standard FFBS within the [spFFBS](#) package. We tailored these with a special consideration for spatiotemporal modeling, referring to Model (8). Algorithm 2 presents the modification to forward filtering (FF) procedure within

Algorithm 3 DYNBPS - weighted backward sampling

Require: Stacking weights $\{\hat{w}^{(t)}\}_{t=1}^T$, filtering parameters and inputs from Algorithm 2

Ensure: R smoothed posterior samples from $\hat{p}(\Theta_{0:T} | \mathcal{D}_T)$

1: **function:** WEIGHTEDBACKSAMP $\left(\{\hat{w}^{(t)}, \{m_t^{(j)}, C_t^{(j)}, \Psi_t^{(j)}, \nu_t^{(j)}, \alpha^{(j)}, \phi^{(j)}\}_{j=1}^J\}_{t=0}^T, R\right)$

2: **for** $r = 1, \dots, R$ **do**

3: *# Draw model \mathcal{M}_j such that $j \sim \text{Multinom}\left(1, J, \{\hat{w}_1^{(T)}, \dots, \hat{w}_J^{(T)}\}\right)$*

4: *# Draw Θ_T from $\text{T}_{p+n,q}(\nu_T^{(j)}, h_T^{(j)}, H_T^{(j)}, \Psi_T^{(j)})$ with $h_T^{(j)} \leftarrow m_T^{(j)}$, $H_T^{(j)} \leftarrow C_T^{(j)}$*

5: **for** $t = T - 1, \dots, 1$ **do**

6: *# Draw model \mathcal{M}_j such that $j \sim \text{Multinom}\left(1, J, \{\hat{w}_1^{(t)}, \dots, \hat{w}_J^{(t)}\}\right)$*

7: *# Draw Θ_T from $\text{T}_{p+n,q}(\nu_T^{(j)}, m_T^{(j)}, C_T^{(j)}, \Psi_T^{(j)})$*

8: *# Compute smoothed posterior parameters*

9: $h_t^{(j)} \leftarrow H_t^{(j)} \left[(C_t^{(j)})^{-1} m_t^{(j)} + G_{t+1}^T (W_{t+1}^{(j)})^{-1} \Theta_{t+1} \right]$

10: $H_T^{(j)} \leftarrow \left[(C_T^{(j)})^{-1} + G_{t+1}^T (W_{t+1}^{(j)})^{-1} G_{t+1} \right]^{-1}$

11: *# Draw Θ_t from $\text{T}_{p+n,q}(\nu_T^{(j)}, h_t^{(j)}, H_t^{(j)}, \Psi_T^{(j)})$*

12: **end for**

13: **end for**

14: **return** R smoothed posterior samples of $\Theta_{0:T}$

15: **end function**

FFBS algorithm for each time instant $t = 1, \dots, T$. In particular, it incorporates Algorithm 1, making its structure different from standard FF, actually retaining most quite similar. It exploits parallel computations, establishing J parallel forward filter flows. This means that the Algorithm 2 implements parallel filtering procedures, where each of these conditions to model \mathcal{M}_j , i.e., uses the couple $\{\alpha_j, \phi_j\}$, for $j = 1, \dots, J$. Once each j -th flow provides filtered posterior distributions, especially the one-step-ahead predictive distribution, we computed DYNBPS weights using Algorithm 1. Prior information is equally used across models \mathcal{M}_j . Then forward propagated for all the observed times. To fully incorporate the new piece of information, as the latest dataset occurs at $T + 1$, it suffices to apply Algorithm 2 once, followed by Algorithm 3 to update posterior sampling with the newest info. This gains advantage from the Markovian dependence assumption between datasets.

In FFBS algorithm presented in Carter and Kohn (1994), backward sampling (BS) passes the information assimilated from all observed T states backward to each time point $t = T - 1, \dots, 1$. This strategy serves to obtain smoothed posterior samples, improving inference by exploiting available future pieces of information. With Algorithm 3 we propose a weighted alternative to the standard backward sampling procedure. For each desired posterior draw $r = 1, \dots, R$, we first sample a model \mathcal{M}_j , with $j = 1, \dots, J$, by giving models weights \hat{w}_T obtained at last observed

time. Then, we draw the posterior sample from the corresponding conditional posterior for Θ_T , i.e. $p(\Theta_T | \mathcal{D}_T, \mathcal{M}_j)$. In doing so, we obtain a sample from the approximated stacked posterior $\hat{p}(\Theta_T | \mathcal{D}_T) = \sum_{j=1}^J \hat{w}_{T,j} p(\Theta_T | \mathcal{D}_T, \mathcal{M}_j)$. For $r = 1, \dots, R$, we use standard BS algorithm backwards, repeating ‘‘model sampling’’ given correspondent weights \hat{w}_t . At the end of the procedure depicted in Algorithm 3, we obtain a smoothed posterior distribution sample of size R . In particular, with Algorithm 3, we smooth out the samples from the stacked (approximated) joint posterior, which can be easily derived as

$$\hat{p}(\Theta_0, \dots, \Theta_T | \mathcal{D}_T) = \hat{p}(\Theta_0 | \Theta_1, \mathcal{D}_T) \hat{p}(\Theta_1 | \Theta_2, \mathcal{D}_T) \cdots \hat{p}(\Theta_{T-1} | \Theta_T, \mathcal{D}_T) \hat{p}(\Theta_T | \mathcal{D}_T), \quad (13)$$

where each $\hat{p}(\Theta_t | \Theta_{t+1}, \mathcal{D}_T) = \sum_{j=1}^J \hat{w}_{t,j} \hat{p}(\Theta_t | \Theta_{t+1}, \mathcal{D}_T, \mathcal{M}_j)$. Together with Algorithm 2, this concludes the Bayesian computation needed to achieve posterior inference and uncertainty quantification for Model (8). Algorithm 4 merges the forward filter and the backward sampling algorithms to give rise to a unified function for the FFBS algorithm using dynamic Bayesian predictive stacking.

We conclude this section by presenting details on two imperative demands in spatiotemporal modeling: temporal forecast and spatial interpolation. The former, given a set of known spatial locations, aim to forecast the future time points given the past, and we focus on one-step-ahead predictive distributions. The latter, given observed data at a specific time point, wants to predict the values of the spatial process for unknown locations. When working with time series, we often aim to forecast the future value of the outcome based on all the information available. Algorithm S1 introduces the Bayesian predictive stacking in the recursive predictive procedure. Following mirrored logic as Algorithm 3, for each posterior predictive sample $r = 1, \dots, R$ we sample a model \mathcal{M}_j based upon \hat{w}_T , i.e. the last set of stacking weights. Then, standard recursive steps for prediction for Bayesian state-space models ensue. Concluding the Algorithm S1, we obtain a stacked posterior predictive sample from $\hat{p}(\tilde{\Theta}_{T+k}, \tilde{Y}_{T+k} | \mathcal{D}_T) = \sum_{j=1}^J \hat{w}_{t,j} p(\tilde{\Theta}_{T+k}, \tilde{Y}_{T+k} | \mathcal{D}_T, \mathcal{M}_j)$ of size R . The recursive part in Algorithm S1 resides in the inner loop. As the one-step ahead predictive depends upon the last observed time, the k -step ahead predictive depends upon the $k-1$ -step ahead, leading

Algorithm 4 DYNBPS - Forward-filter-backward-sampling

Require: Data $\mathcal{D}_{1:T}$, observation and state transition matrices $F_{1:T}, G_{1:T}$, starting stacking weights $\hat{w}^{(0)}$, hyperparameters $\left\{m_0^{(j)}, C_0^{(j)}, \Psi_0^{(j)}, \nu_0^{(j)}, \alpha^{(j)}, \phi^{(j)}\right\}_{j=1}^J$

Ensure: R smoothed posterior samples from $\hat{p}(\Theta_{0:T} | \mathcal{D}_T)$

- 1: **function:** DYNBPS-FFBS $\left(\mathcal{D}_{1:T}, F_{1:T}, G_{1:T}, \hat{w}^{(0)}, \left\{m_0^{(j)}, C_0^{(j)}, \Psi_0^{(j)}, \nu_0^{(j)}, \alpha^{(j)}, \phi^{(j)}\right\}_{j=1}^J, R\right)$
- 2: PFF-OUT \leftarrow PARALLELFORWFILT $\left(\mathcal{D}_{1:T}, F_{1:T}, G_{1:T}, \hat{w}^{(0)}, \left\{m_0^{(j)}, C_0^{(j)}, \Psi_0^{(j)}, \nu_0^{(j)}, \alpha^{(j)}, \phi^{(j)}\right\}_{j=1}^J\right)$
- 3: WBS-OUT \leftarrow WEIGHTEDBACKSAMP $\left(\left\{\hat{w}^{(t)}, \left\{m_t^{(j)}, C_t^{(j)}, \Psi_t^{(j)}, \nu_t^{(j)}, \alpha^{(j)}, \phi^{(j)}\right\}_{j=1}^J\right\}_{t=0}^T, R\right)$
- 4: **return** WBS-OUT
- 5: **end function**

to the need to compute all the previous $k - 1$ predictive distributions, to obtain the k -step ahead uncertainty quantification. The prediction will worsen with the length of the forecast horizon k , leading to an increasing diffusion for the posterior predictive distribution. This retraces ARIMA predictive behavior, where the posterior mean converges to the global mean, i.e., the mean-reverting property, while the variance shows linear dependence on k .

Spatial interpolation, also called spatial prediction, helps improve decision-making and problem-understanding when spatial components play a fundamental role, e.g., environmental and climate sciences, medical screenings, etc. It allows us to infer spatial process characteristics and spatial distribution over unobserved locations, and possibly at any point within the region of interest. Letting $\mathcal{U} = \{u_1, \dots, u_m\}$ be the set of m unmonitored locations as specified in Section 2. In Equation (10) we derive the joint posterior predictive for the response \tilde{Y}_t , and the spatial process $\tilde{\Omega}_t$ over \mathcal{U} , at any generic fixed time point $t = 1, \dots, T$. The algorithm S2 provides a practical procedure that incorporates dynamic Bayesian predictive stacking into spatial prediction to draw posterior predictive samples from the stacked predictive distribution $\hat{p}(\tilde{Y}_t, \tilde{\Omega}_t | \mathcal{D}_t) = \sum_{j=1}^J \hat{w}_{t,j} p(\tilde{Y}_t, \tilde{\Omega}_t | \mathcal{D}_t, \mathcal{M}_j)$, at any $t \in \mathcal{T}$. Again, Algorithm S2 starts sampling models \mathcal{M}_j using weights \hat{w}_t . Then we compute the parameters of the corresponding conditional predictive posterior distribution $p(\tilde{Y}_t, \tilde{\Omega}_t | \mathcal{D}_t, \mathcal{M}_j)$, and draw a predictive sample. This must be repeated for the number R of desired predictive samples, as with Algorithm S1. After completing the sampling procedure, we can perform uncertainty quantification for the outcomes and the spatial processes across the entire region of interest, perhaps providing interpolated spatial maps.

4 Simulations experiment

We highlight the potential of dynamic Bayesian predictive stacking under different simulation experiments, while posing challenges and exploring features of multivariate spatiotemporal analysis. We have developed an efficient and effective approach to managing online spatiotemporal learning for massive georeferenced historical data within the `Rcpp`-based `spFFBS` package. The simulations and analysis were implemented using native `R` and `C++` programming languages. Reproducibility is guaranteed by access to the public repository <https://github.com/lucapresicce/lucapresicce/Markovian-Spatiotemporal-Propagation>, which provides all the programs required to replicate results. We obtain the results by using just a standard laptop running an Intel Core i7-8750H CPU with 5 cores for parallel computation, with 16 GB of RAM, representing the efficiency of DYNBPS within scarce computational resources frameworks. Details on programs and Algorithms are explored extensively in Section 3.

4.1 Amortized Bayesian forecast

We supervise an AI algorithm using DYNBPS outputs to deliver amortized Bayesian forecasts for spatiotemporal data analysis. We train an artificial intelligence model to forecast three one-step-ahead posterior predictive distribution quantiles (i.e., 50, 2.5, and 97.5) for the multivariate spatial response Y and the spatial process Ω . This experiment aims to represent the effectiveness of DYNBPS as a supporting statistical learning tool for modern AI systems.

We generate 100 instances of Y from (8) using a fixed realization of Θ for $q = 2$ correlated outcomes, over $t = 10$ time points, $n = 500$ spatial locations that remain fixed across the datasets, and a fixed design matrix X with $p = 2$ comprising an intercept and a single predictor whose values were sampled independently from a uniform distribution over $[-1, 1]$. The true multivariate spatial process Ω and the regression coefficients B were fixed and evolved according to the state equation. The starting value for $\Theta_0 = [B_0^T : \Omega_0^T]^T$ was drawn from its prior distribution; see Section 2.1. We then fixed the column covariance matrix as $\Sigma = \begin{bmatrix} 1 & -0.3 \\ -0.3 & 1 \end{bmatrix}$, while setting $\alpha = 0.8$, and $\rho_\phi(s_i, s_j) = \exp(-\phi\|s_i - s_j\|)$ with $\phi = 4$.

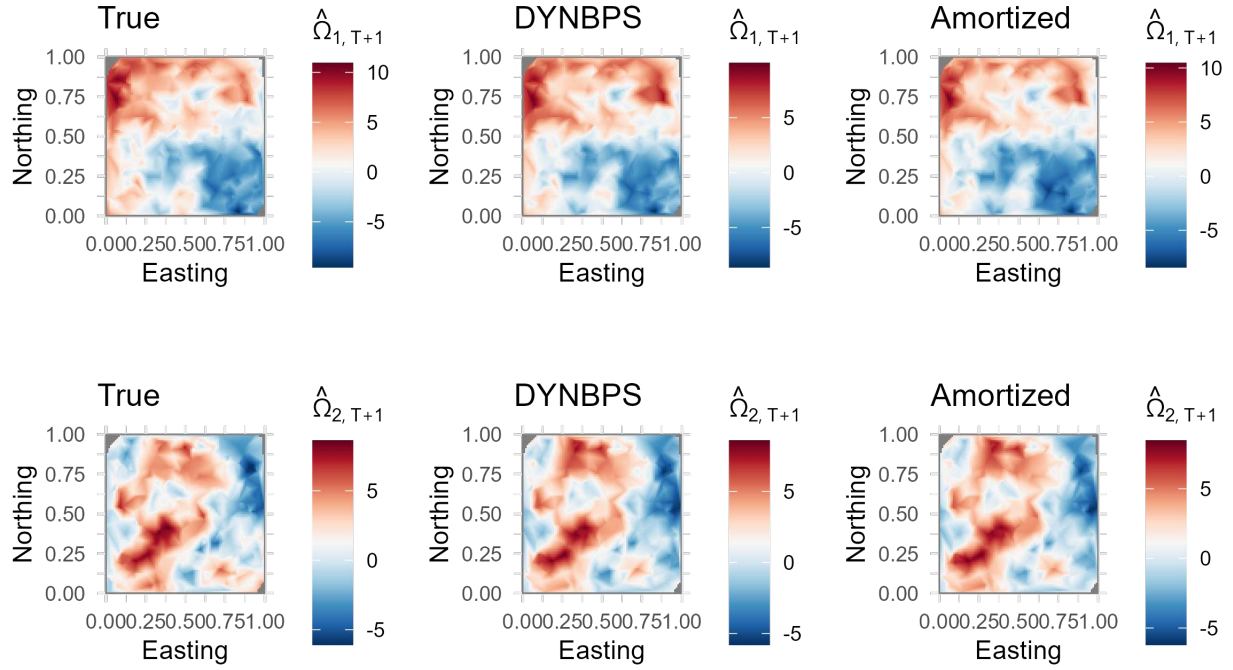


Figure 3: Spatial process Ω one-step ahead forecast surface interpolations: true spatial process Ω (leftmost column), 50-th quantile DYNBPS forecast (center column), 50-th quantile amortized forecast (rightmost column); each row corresponds to a different outcome in Ω

These yield 100 simulated pairs $\{Z^{(i)}, W^{(i)}\}$ that we use to supervise the training of the neural network g_ψ , characterized by the set of parameters ψ . Each $Z^{(i)} = [Y : P] \in \mathbb{R}^{n \times (q+p+n)}$ and each $W^{(i)} \in \mathbb{R}^{n \times (2q+3)}$ comprises the $\{2.5, 50, 97.5\}$ one-step-ahead posterior predictive quantiles for the distinct elements of $\{Y_{T+1}, \Omega_{T+1}\}$, for $i = 1, \dots, 100$. We derive posterior predictive quantiles in each $W^{(i)}$ using $R = 200$ posterior samples by applying DYNBPS to each generated dataset $Z^{(i)}$ with $\alpha \in \{0.7, 0.8, 0.9\}$ and $\phi \in \{2, 4, 6\}$, characterizing $J = 9$ parallel learning flows.

We implemented a recurrent neural network (RNN) (Werbos, 1990) framework in R using the `keras` (Kalinowski et al., 2024) and `tensorflow` (Allaire et al., 2024) backends for native Python. The neural architecture consists of a Gated Recurrent Unit (GRU) (Cho et al., 2014) encoder with 64 hidden units to capture temporal dependencies, followed by a fully connected dense layer with 128 RELU-ACTIVATED neurons to perform nonlinear feature transformations. The final linear output layer projects the latent representation to the desired dimension. Overall, the network $g_\psi(\cdot)$ comprises approximately 49 million parameters, collected in ψ .

The recurrent network is trained over 100 epochs (with 32 batches per epoch) by minimizing $\hat{\psi} = \arg \min_\psi 1/N \sum_{i=1}^N L(g_\psi(X_i), Z_i)$ implemented in `Keras` using the Adam optimizer with mean

squared error (MSE) loss $L(\cdot, \cdot)$. For evaluation, we apply the trained model to unseen datasets with the same dimensions. Performance is assessed using the root mean squared prediction (RMPSE) error for the median. Figures S8,3 display the forecasted posterior predictive for Y_{T+1} and Ω_{T+1} quantiles, respectively. We compare the results from the amortized Bayesian forecast with the true surfaces and the DYNBPS prediction for the 50th quantile, presented in the first and second columns of each figure, respectively. The amortized forecasts achieve striking results with minimal computational effort, closely matching outcomes from DYNBPS. This shows how prediction performance can even benefit from knowledge transfer from DYNBPS to AI models, notwithstanding the amortization of neural posterior forecasts.

This experiment aims to show the strengths of amortized inference and transfer learning working together. Once trained, the AI model provides instant posterior predictive quantile estimates for new datasets, without requiring re-running DYNBPS, thus amortizing the computational cost across future forecast tasks. Additionally, the model generalizes across a range of data-generating conditions, effectively enabling posterior predictive transfer to new but structurally similar problems. This makes the approach especially useful in large-scale or resource-constrained applications where repeated full Bayesian inference would be prohibitively expensive.

4.2 Model class influence

We explore how dynamic BPS behaves in the \mathcal{M} -closed and \mathcal{M} -open settings. Generally, these two classes of model misspecifications relate to opposite scenarios. The \mathcal{M} -closed refers to the case when the true model can be identified within a finite set of candidate models. \mathcal{M} -open class admits the existence of the true models, but this cannot be directly specified within candidate models.

Hereafter, model specification is characterized by values of α and ϕ , where the data generating values $\{\alpha = 0.8, \phi = 4\}$ represent the true model (TRUE). The dynamic BPS was tested over \mathcal{M} -closed and \mathcal{M} -open settings. For DYNBPS under closed settings (DYNBPS-C), we specify $J = 9$ competitive models with $\alpha \in \{0.7, 0.8, 0.9\}$ and $\phi \in \{2, 4, 6\}$ that yield effective spatial ranges as a percentage of the maximum point inter-distance of 105%, 53%, 35%, respectively, including the true model as one of the possible candidates. Conversely, in the \mathcal{M} -open setting, even though the true

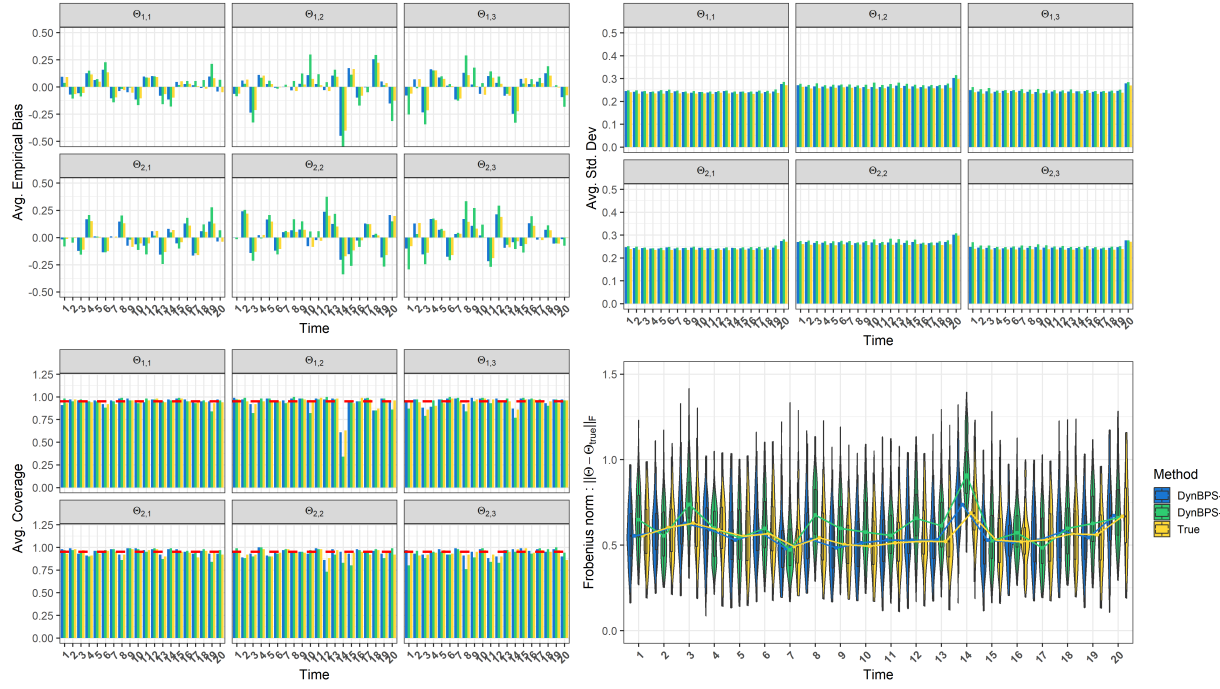


Figure 4: Posterior metrics at each time point for regression coefficients B , i.e. $\Theta_{1,p,1:q}$, under the considered model configurations and 50 replications: average empirical bias (top left), average posterior standard deviation (top right), average credible interval coverage (bottom left), Frobenius norm distribution (bottom right)

model exists, it cannot be fully specified. Thus, for dynamic BPS under the open setting (DYNBPS-O), we randomly define $J = 9$ candidate models. In particular, we uniformly sample 3 values for $\alpha \in (0.5, 1)$ and 3 values for $\phi \in [1, 50]$. We perform the experiment using 25 replications.

Each replicate consists of values of $n \times q \times t$ outcome Y generated from (8) with $n = 100$, $q = 3$, $t = 20$ and $p = 2$, X includes two predictors generated from a standard uniform distribution over $[0, 1]$, $\Sigma = \begin{bmatrix} 1 & -0.3 & 0.6 \\ -0.3 & 1.2 & 0.4 \\ 0.6 & 0.4 & 1 \end{bmatrix}$. $\Theta = [B^T : \Omega^T]^T$ was defined by allowing the system to evolve in (8), starting with a realization from the marginal prior distribution. We defined the joint prior distribution for all model \mathcal{M}_j regarding Θ, Σ from the matrix-normal inverse Wishart family, with parameters $m_0 = 0_{p+n \times q}$, $C_0 = \begin{bmatrix} 0.05\mathbb{I}_p & 0 \\ 0 & \mathcal{R}(\mathcal{S}, \mathcal{S}; \phi=1) \end{bmatrix}$, $\Psi_0 = 10\mathbb{I}_q$, and $\nu_0 = q + 1$.

The $n \times n$ spatial correlation matrix V is specified using an exponential correlation function with $\phi = 4$ and $\alpha = 0.8$.

Every column in Figure S10 shows predictive sampling metrics for each simulated outcome. Rows show (i) absolute bias; (ii) mean squared prediction error (MSPE); (iii) predictive interval width; and (iv) predictive variance. We report boxplots for the distribution of each metric across the 50 replicates at any instant in the horizon, i.e., future time points. In terms of predictive MSPE and absolute bias, we notice equivalent results among the settings, indicating excellent predictive

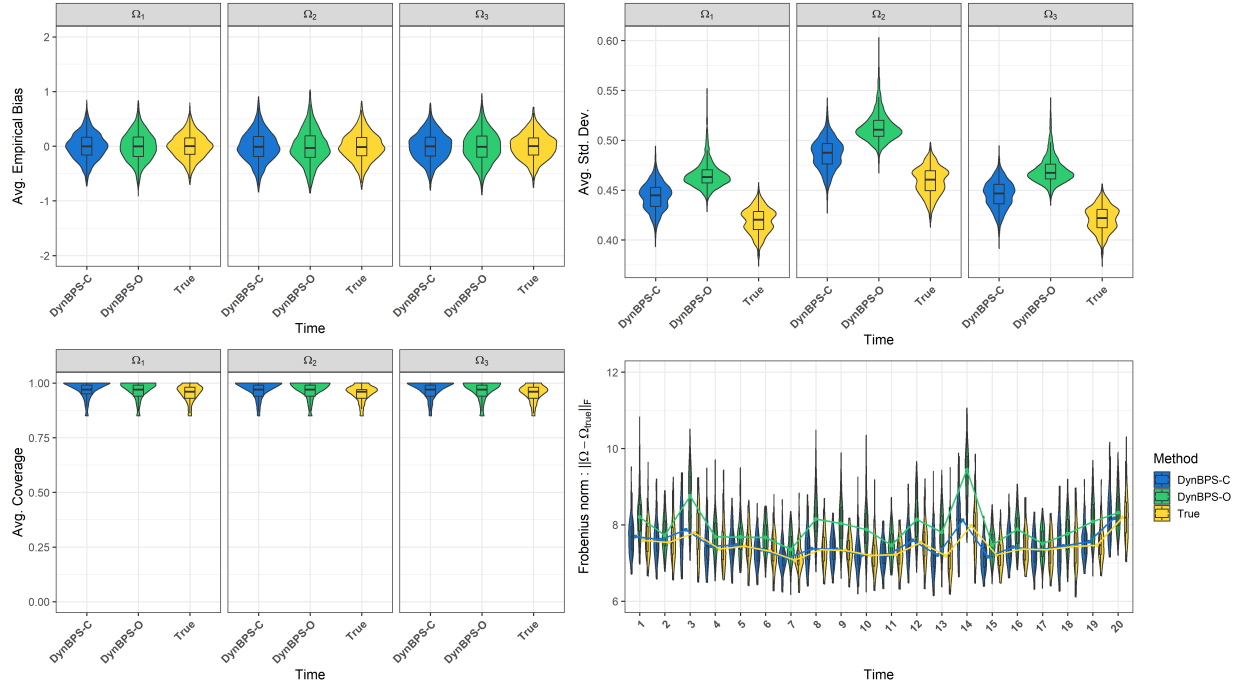


Figure 5: Posterior metrics at each time point for each component of the multivariate spatial process Ω , under the considered model configurations and 50 replications: average empirical bias (top left), average posterior standard deviation (top right), average credible interval coverage (bottom left), Frobenius norm distribution (bottom right)

aptitude of dynamic BPS, regardless of whether the case is closed or open. Soft differences emerge with respect to predictive interval width and variance. Expectedly, the \mathcal{M} -open setting induces greater variability in predictive distributions, even though it is largely comparable with the \mathcal{M} -closed setting. In fact, predictive variability inflates when we introduce uncertainty in $\{\alpha, \phi\}$.

The series of Figures 4,5,S11 aims to provide insight into the posterior inference achieved by DYNBPS when comparing \mathcal{M} -closed and \mathcal{M} -open settings. Every figure displays four panels: (i) average empirical bias; (ii) average coverage; (iii) average posterior standard deviation; and (iv) Frobenius norm distribution across the 50 replicates.

Starting from time-dependent parameters, Figure 4 mainly shows which regression coefficient submatrix B_t is well-identified from DYNBPS. The bottom-right sub-panel includes the distributions over replications at any time point t for any setting of the Frobenius norm, i.e., $\| \hat{B}_t - B_t \|_F = \sqrt{\sum_{i=1}^p \sum_{j=1}^q | \hat{\beta}_{i,j,t} - \beta_{i,j,t} |^2}$, where \hat{B}_t and $\hat{\beta}_t$ represent the maximum a posteriori (MAP) estimate of B and its element $\beta_{i,j}$. We support the interpretation using a different colored line for each setting, representing the median of the Frobenius norm distribution across time points. Looking at the average coverage (top-right) and Frobenius norm (bottom-right) subplots, we record a unique exception at time $t = 14$: all the evaluated models produce the worst estimates. Nevertheless, the

replication results are generally balanced among settings for the considered metrics. \mathcal{M} -open stands out in terms of empirical bias and Frobenius norm, but the differences are numerically negligible. This is somewhat expected when working with \mathcal{M} -open settings, especially given the simulation setting: we sampled a different set of values for $\{\alpha, \phi\}$ across replications. This inevitably inflates variability and shifts into diffusion metrics. Different from Figure 4, which reports a panel for each element of B ; Figure 5 collects data for each of the $q = 3$ components of the multivariate spatial process. Thus, the only subpanel that is time-dependent reflects Frobenius norm distributions (still bottom-right), similar to the bottom-right subplot of Figure 4. Here, there is a net separation between \mathcal{M} -open and other settings, which perform more stably. Indeed, the median-trace for \mathcal{M} -open settings shows sensibly greater values. However, in terms of average empirical bias (top-left) and average coverage (bottom-left), \mathcal{M} -close and \mathcal{M} -open performances are indistinguishable, ensuring good inferential achievements. While the average standard deviation results (top-right) mirror the behavior of the underlying subpanel: \mathcal{M} -close stays “closer” to the true model in terms of estimates’ diffusion, “setting” distance from \mathcal{M} -open setting. Figure 5 displays effective recovery of the true multivariate spatial-dependence among the q outcomes, across time. DYNBPS provides excellent uncertainty quantification for either \mathcal{M} -closed or \mathcal{M} -open settings.

Finally, we gather results on the dense covariance matrix Σ , which captures the multivariate non-spatial dependence among the q variables. We divided Figure S11 into two columns. We compose the left-most column by stacking three metrics vertically: (i) average empirical bias; (ii) average coverage; and (iii) average standard deviation, separately represented by its elements, i.e., $\Sigma_{i,j}$ for $i, j = 1, \dots, q$. In the rightmost column, we report the Frobenius norm distribution across replications for each setting. Figures 4 and 5 show time-dependent objects. Here, we only have a distribution by setting, where the posterior distribution at the last observed time is considered to compute the MAP estimates. The latter reflects something already seen for B and Ω : DYNBPS-O inflates variability in the estimates. However, for regression coefficients and the multivariate spatial process, the greater diffusion of the estimates does not affect the inferential performances, such as the empirical bias and the coverage; here, it does. The average coverage (middle-left) suffers from undercoverage, in equal measure for all the parameters. Even though differences are negligible, as it

attests to having an average coverage of about 90%, it is worth noting. Similar traits are reflected by the average empirical bias, which diverges from that achieved by other settings. Notwithstanding the great achievement of dynamic BPS, we are not surprised that the worst inferential performances are related to the common-covariance matrix Σ . Indeed, when working with georeferenced data, it is well-known that covariances are not identifiable from data realizations (Zhang, 2004), especially when the data shows multidimensional dependencies. These findings are consistent with Stein (1988) and Stein and Handcock (1989), who theoretically established the ability of Gaussian processes to deliver good predictive performance even for misspecified covariance functions in fixed domains.

5 Case study results

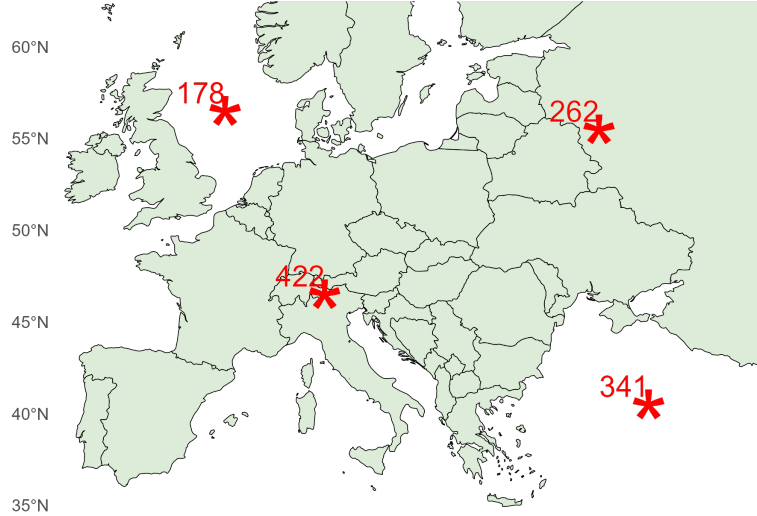
The Copernicus Data Space Ecosystem (CDSE) is an open, cloud-based ecosystem for Earth observation data, providing free and instant access to data from the Copernicus Program, especially the Sentinel satellites, along with tools for processing and analysis. It serves as a central platform that enables users, from researchers to developers, to explore, access, and process Earth data for various applications, supporting the development of new value-added services. The Copernicus Program aims to deliver geo-spatial data products, along with accompanying statistical and machine learning tools, in a widely accessible manner to drive positive change and preserve the planet.

Easy accessibility to such data generates scientific questions relevant to how underlying processes manifest themselves in observed data and, more specifically, the role of different types of associations in such manifestations. Access to massive volumes of data, along with accompanying machine learning tools, requires statistical models that are congruent with frameworks driven by Artificial Intelligence (AI). We analyze four key Copernicus variables that are associated with each other and vary over space and time: 2-meter air temperature (degrees Celsius degrees), total monthly precipitation (mm), 10-meter wind speed (ms^{-1}), and monthly evaporation (mm). These variables collectively represent essential surface climate processes that are relevant to hydrology, energy balance, and atmospheric dynamics.

Our statistical modeling approach incorporated a spatiotemporal regression structure in which we included monthly cloud-coverage percentage (in %), monthly surface solar radiation (in $W m^{-2}$,

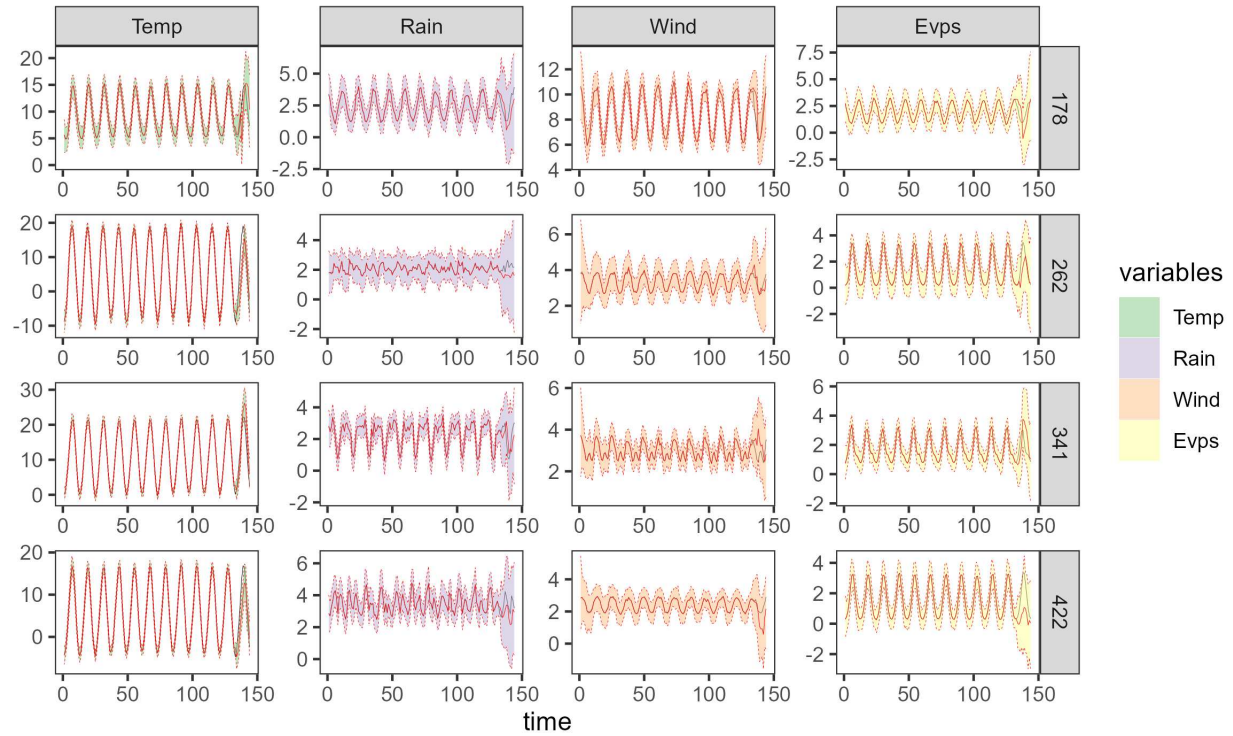
representing the monthly mean incident shortwave radiation on a horizontal surface), monthly sea-level pressure (in hPa), and monthly near-surface specific humidity (in g kg^{-1} , representing the monthly amount of moisture in the air near the surface divided by the total mass of air plus moisture) as predictors to control for broad-scale environmental variability. We focus our analysis of four key climate variables of interest on the European region bounded by latitudes 30° , 60°N and longitudes -10° , 40°E , using complete monthly records from December 2002 to December 2014, which is the latest available data point with full variable coverage. This yields $T = 144$ time points, of which the last $h = 24$ months are held for predictive evaluation, leaving 120 months to comprise a learning set. From this spatiotemporal domain, we use $n = 500$ regularly distributed locations for training and keep an additional 100 locations to assess spatial interpolation, aggregated for $q = 4$ response variables. The resulting data consist of $500 \times 120 \times 4 = 240,000$ spatiotemporal observations. The maximum inter-site distance among the monitored locations is approximately 6,320 kilometers. An extensive exploratory data analysis accompanies this dataset, offering a detailed characterization of its spatiotemporal dependence structure (see Appendix D).

The use of these covariates to control for the large-scale atmospheric driver factors is widely supported in the literature for modeling climate response variables (see e.g., [Jacobs et al., 2009](#); [Tramblay et al., 2011](#); [van Osnabrugge et al., 2019](#); [Felsche and Ludwig, 2021](#); [Chen et al., 2024](#)). We omit an intercept term deliberately, as we introduce seasonal dummy variables. To account for seasonal effects, we apply structural modifications to the matrices F_t and G_t . As we observed monthly seasonality in the outcomes, at any time instant t we define $F_t = [X_t : \Delta_t : \mathbb{I}_n]$, where $\Delta_t = [\delta_{1,t}, \dots, \delta_{11,t}]$, and each of $\delta_{i,t} = \mathbf{1}_{(i=t)}(i)$, i.e., $\delta_{i,t}$ is a vector of ones when the month at time point t is the same as i . Then, we removed the intercept from X_t , and we incorporate monthly dummy variables, such that $\tilde{X}_t = [X_t : \Delta_t] = [x_{1,t}, x_{2,t}, \delta_{1,t}, \dots, \delta_{11,t}]$, specifying 11 variables to ensure full rank for \tilde{X}_t and $F_t = [\tilde{X}_t : \mathbb{I}_n]$, corresponding to total number of predictors $p = 13$. This led to the following formulation for $\Theta_t = [B_t : S_t; \Omega_t]$, where S_t represent the $(m - 1) \times q$ matrix of seasonal effect. While G_t only needs an augmentation of its dimension, which is intrinsic passing from X_t to \tilde{X}_t in Models (8) For the spatial covariance function at any month, we choose to use an exponential kernel, which reflects the spatial process smoothness typically observed over



10°W 0° 10°E 20°E 30°E 40°E

(a) Randomly selected locations over the central Europe region



(b) One-step ahead forecasts reporting: MAP (red solid line), 95% credible interval (red dashed line), and ground truth (black solid line), for selected points

Figure 6: One-step ahead average monthly forecast for selected spatial points

large-scale domains. The temporal structure via monthly indexing enables the model to learn seasonal and interannual dynamics; this setup facilitated both interpolation and prediction tasks within a coherent statistical framework. We implement a fully automated procedure setting the grid of values for $\{\alpha, \phi\}$, which makes use of spatiotemporal variograms, see Appendix S4. The process ends by providing $J = 4$ candidate models: the variogram estimate missing nugget for

the outcomes, then it automatically fixes $\alpha = 0.999$, while letting vary the range parameter as $\phi \in \{0.180, 0.212, 0.229, 0.308\}$. The prior distribution was set to non-informative choices, typically used when working with matrix-variate models in spatial analysis (see e.g., [Zhang and Banerjee, 2022](#); [Presicce and Banerjee, 2024](#)). We give on Θ, Σ a matrix-normal inverse Wishart prior, where parameters were fixed as: $m_0 = 0_{(p+n) \times q}$, $C_0 = \begin{bmatrix} \mathbb{I}_p & 0_{p \times n} \\ 0_{n \times p} & \mathcal{R}_0(\mathcal{S}, \mathcal{S}; \phi=1) \end{bmatrix}$, opting for an exponential spatial correlation function, and $\nu_0 = q$, $\Psi_0 = \mathbb{I}_q$.

We train the model over the entire observed multivariate time series and then conduct one-step-ahead forecasting for the full temporal sequence, including both observed and unobserved time points. The model demonstrated excellent predictive performance, with forecast values nearly indistinguishable from the held-out observations. Forecast performance was evaluated over the full time series for each of the four variables. Please see Figure 6, which demonstrates highly accurate predictive behavior, with forecast trajectories closely matching ground-truth values for a random selection of equally spaced points over Europe. Forecast surfaces are then illustrated for a selection of time points, one for each variable: (i) Figure S12 for air temperature; (ii) Figure S13 for rain precipitation; (iii) Figure S14 for wind speed; and (iv) Figure S15. The results from these Figures are clear: DYNBPS achieved striking forecast performance, exactly mimicking the observed multivariate spatiotemporal process. In addition to temporal forecasting, we performed spatial interpolation at 100 out-of-sample withheld locations. We conducted spatial prediction at observed time points (in-sample) and at future unobserved times (out-of-sample), providing a robust assessment of the model's ability to generalize spatial interpolation beyond its learning set. Multivariate interpolated maps exhibited smooth gradients and high alignment with known climatological patterns, suggesting that the model accurately captures both temporal variability and spatial structure. Figure S16 presents interpolated surfaces for a selected observed time slice (September 2007) for all four variables (right panel), in comparison to observed interpolated fields (left panel). Similarly, Figure 7 reports spatial predicted maps for a selected out-of-sample month (September 2013) against observed spatial surfaces (right to left). The left panel of Figure 6 shows the exact georeference for each of the points we include in the temporal series forecast in the right panel. As expected, out-of-sample 1-step-ahead predictions turn out to be characterized by greater

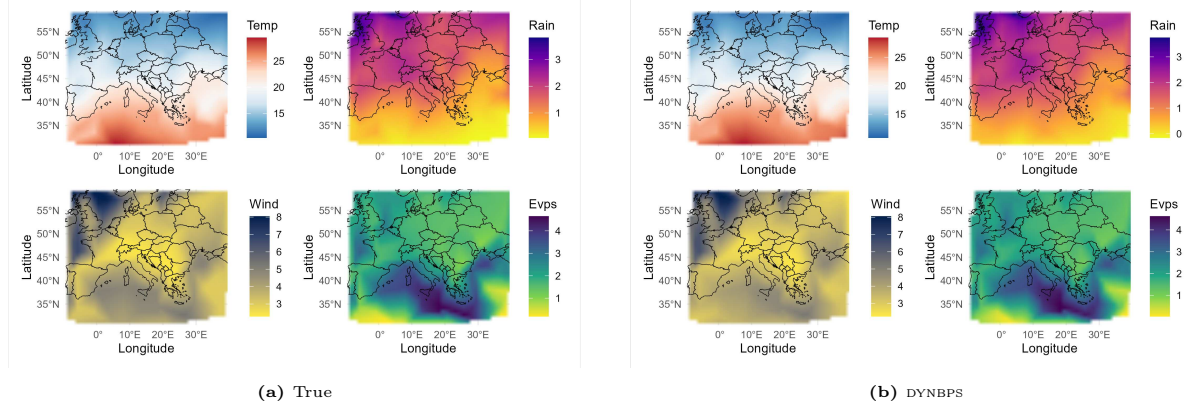


Figure 7: Spatial surface interpolation at unobserved time (out of sample)

variability for predictive intervals, even though the empirical coverage reports very good results. Notwithstanding, state-space models usually provide predictive intervals that grow linearly with t ; in this case, DYNBPS offer a different behavior, as the maximum width reaches an upper bound. This would be interesting to investigate, and we left it for future research. For any of the considered points, the model retraces the truth very closely, seizing the seasonality and providing striking extrapolations.

Both sets of interpolated fields prove the excellent spatial prediction achieved by dynamic Bayesian predictive stacking. In addition, as we intentionally selected the same month for in-sample and out-of-sample interpolation, i.e., September, we can compare Figure S16 with Figure 7. They actually show extreme similarities, implying how the model can learn spatial patterns without losing seasonal coherence.

Together, these results validate the pattern identified by the c3s Atlas dataset for large-scale spatiotemporal analysis in climate research and demonstrate the scalability of DYNBPS for joint multivariate forecasting and interpolation tasks across the entire European continent.

Dynamic BPS brings the feasibility of combining physically interpretable multidimensional factors with data-driven spatiotemporal modeling to a new level, supporting climate monitoring and decision-making within GeoAIsystems. Indeed, the entire Bayesian estimation framework only takes nearly 12 minutes to provide posterior and posterior predictive sampling, along with uncertainty quantification. This occurs on a standard laptop, with very limited resources, as explained in Section 3; allowing almost-automated multivariate spatiotemporal Bayesian modeling for large-scale settings in constrained GeoAIs systems.

6 Discussion

We have devised a spatiotemporal statistical model tailored to readily analyze large-scale problems, minimizing user effort. The contribution harnesses analytically accessible matrix-variate statistical distributions in conjunction with a novel introduction: the dynamic Bayesian predictive stacking. The DYNBPS deliver prompt inference by avoiding simulation-based algorithms that often require extensive human tuning. Our proposed spatiotemporal dynamic modeling approach relies on Markovian propagation across spatial datasets through a modification of the standard FFBS procedure to process massive amounts of online spatial data on high-performance CPU architectures. Nevertheless, DYNBPS demonstrate extremely useful computational features even for limited architectures. Some additional remarks are warranted. The development here has been elucidated with a hierarchical matrix-variate spatiotemporal process within dynamic linear model frameworks. Although modeling simplifications have been introduced to minimize human intervention, we emphasize that DYNBPS seamlessly apply to more versatile but analytically intractable models.

Future research can build upon recent work by [Tallman and West \(2023\)](#); [Cabel et al. \(2025\)](#) to enrich spatiotemporal dependence structures within DYNBPS and further accelerate amortized inference. We are also planning to study and introduce concepts from Bayesian predictive synthesis ([McAlinn and West, 2019](#); [McAlinn et al., 2020](#)) into dynamic Bayesian predictive stacking, thereby enlarging the class of solvable problems without compromising uncertainty quantification on any spatial hyperparameters. Disseminating our proposed product with our accompanying software, which is currently being migrated to `R`, is expected to significantly boost dynamic spatiotemporal modeling. Future directions will also explore the perceived potential of DYNBPS as a feeder for emerging amortized inference methods ([Ganguly et al., 2023](#); [Zammit-Mangion et al., 2024](#); [Sainsbury-Dale et al., 2024](#)) to achieve Bayesian inference. Rapid delivery of posterior estimates of the entire spatiotemporal process from DYNBPS will provide more training data for amortized neural learners, which can result in accelerated tuning for subsequent Bayesian inference. We do not see our proposed approach as a competitor to, but rather as supplementary to, amortized neural inference.

Supplementary Materials

The online supplement includes derivations and theoretical details on dynamic Bayesian predictive stacking (Section S1), computational methods and algorithms (Section S2), supplementary simulation experiment results (Section S3), exploratory data analysis, and automated hyperparameter settings (Section S4), and additional graphics (Section S5). All computer programs required to reproduce the analysis are publicly accessible at the GitHub repository <https://github.com/lucapresicce/Markovian-Spatiotemporal-Propagation>.

References

Abdalla, N., S. Banerjee, G. Ramachandran, and S. Arnold (2020). Bayesian state space modeling of physical processes in industrial hygiene. *Technometrics* 62(2), 147–160.

Ali, M. M. (1979, December). Analysis of stationary spatial-temporal processes: Estimation and prediction. *Biometrika* 66(3), 513–518.

Allaire, J. J., T. Kalinowski, D. Falbel, D. Eddelbuettel, Y. Tang [aut, cph, N. Golding, G. I. E. Tutorials), , Posit, and PBC (2024, April). tensorflow: R Interface to 'TensorFlow'.

Banerjee, S. (2020). Modeling massive spatial datasets using a conjugate Bayesian linear modeling framework. *Spatial Statistics* 37, 100417.

Banerjee, S., X. Chen, I. Frankenburg, and D. Zhou (2025). Dynamic Bayesian Learning for Spatiotemporal Mechanistic Models. *Journal of Machine Learning Research* 26(146), 1–43.

Banerjee, S., A. E. Gelfand, and B. P. Carlin (2025, September). *Hierarchical modeling and analysis for spatial data* (3 ed.). London, England: Chapman and Hall.

Breiman, L. (1996). Stacked Regressions. *Machine Learning* 24(1), 49–64.

Cabel, D., S. Sugasawa, M. Kato, K. Takanashi, and K. McAlinn (2025, January). Bayesian Spatial Predictive Synthesis. arXiv:2203.05197 [stat].

Carter, C. K. and R. Kohn (1994, September). On Gibbs sampling for state space models. *Biometrika* 81(3), 541–553.

Chen, L., X. Zhong, H. Li, J. Wu, B. Lu, D. Chen, S.-P. Xie, L. Wu, Q. Chao, C. Lin, Z. Hu, and Y. Qi (2024, July). A machine learning model that outperforms conventional global subseasonal forecast models. *Nature Communications* 15(1), 6425.

Chen, Q., R. Han, F. Ye, and W. Li (2011). Spatio-temporal ecological models. *Ecological Informatics* 6(1), 37–43.

Cho, K., B. van Merriënboer, C. Gulcehre, D. Bahdanau, F. Bougares, H. Schwenk, and Y. Bengio (2014, October). Learning Phrase Representations using RNN Encoder–Decoder for Statistical Machine Translation. In A. Moschitti, B. Pang, and W. Daelemans (Eds.), *Proceedings of the 2014 Conference on Empirical Methods in Natural Language Processing (EMNLP)*, Doha, Qatar, pp. 1724–1734. Association for Computational Linguistics.

Cooper, A., D. Simpson, L. Kennedy, C. Forbes, and A. Vehtari (2023). Cross-validatory model selection for Bayesian autoregressions with exogenous regressors. *arXiv preprint*. arXiv:2301.08276 [stat.ME].

Cressie, N. A. C. and C. K. Wikle (2011). *Statistics for spatio-temporal data*. Wiley series in probability and statistics. Hoboken, N.J: Wiley.

Czaran, T. and S. Bartha (1992, February). Spatiotemporal dynamic models of plant populations and communities. *Trends in Ecology & Evolution* 7(2), 38–42.

Elkhouly, M. and M. A. R. Ferreira (2021). Dynamic multiscale spatiotemporal models for multivariate Gaussian data. *Spatial Statistics* 41, 100475.

Felsche, E. and R. Ludwig (2021, December). Applying machine learning for drought prediction in a perfect model framework using data from a large ensemble of climate simulations. *Natural Hazards and Earth System Sciences* 21(12), 3679–3691.

Gamerman, D., H. F. Lopes, and E. Salazar (2008). Spatial dynamic factor analysis. *Bayesian Analysis* 3(4), 759 – 792.

Ganguly, A., S. Jain, and U. Watchareeruetai (2023, October). Amortized Variational Inference: A Systematic Review. *Journal of Artificial Intelligence Research* 78, 167–215.

Gelfand, A. E., S. Banerjee, and D. Gamerman (2005). Spatial process modelling for univariate and multivariate dynamic spatial data. *Environmetrics* 16(5), 465–479.

Gelfand, A. E., P. Diggle, P. Guttorp, and M. Fuentes (2010). *Handbook of Spatial Statistics*. Taylor & Francis.

Gneiting, T. and A. E. Raftery (2007). Strictly Proper Scoring Rules, Prediction, and Estimation. *Journal of the American Statistical Association* 102(477), 359–378.

Hefley, T. J., M. B. Hooten, E. M. Hanks, R. E. Russell, and D. P. Walsh (2017). Dynamic spatio-temporal models for spatial data. *Spatial Statistics* 20, 206–220.

Idjigbèrou, S. E., E. S. P. Assédé, S. Biaou, G. N. Gouwakinnou, A. K. Natta, and S. S. H. Biaou (2025). Spatio-temporal dynamics of Isoberlinia-dominated woodlands in disturbance-prone landscapes over 15 years. *Global Ecology and Conservation* 59, e03512.

Ivanovic, B. and M. Pavone (2019, October). The Trajectron: Probabilistic Multi-Agent Trajectory Modeling With Dynamic Spatiotemporal Graphs. In *Proceedings of the IEEE/CVF International Conference on Computer Vision (ICCV)*.

Jacobs, J. M., B. Lowry, M. Choi, and C. H. Bolster (2009, March). GOES Solar Radiation for Evapotranspiration Estimation and Streamflow Prediction. *Journal of Hydrologic Engineering* 14(3), 293–300.

Jiménez, J. C. and C. A. d. B. Pereira (2021). Assessing dynamic effects on a Bayesian matrix-variate dynamic linear model: An application to task-based fMRI data analysis. *Computational Statistics & Data Analysis* 163, 107297.

Kalinowski, T., D. Falbel, J. J. Allaire, F. Chollet, RStudio, Google, Y. Tang [ctb, cph, W. V. D. Bijl, M. Studer, and S. Keydana (2024, April). keras: R Interface to 'Keras'.

Kennedy, L., A. Vehtari, and A. Gelman (2024). Model validation for aggregate inferences in out-of-sample prediction. *arXiv preprint*. arXiv:2312.06334 [stat.ME].

Landim, F. and D. Gamerman (2000). Dynamic hierarchical models: an extension to matrix-variate observations. *Computational Statistics & Data Analysis* 35(1), 11–42.

McAlinn, K., A. , Knut Are, N. , Jouchi, , and M. West (2020, July). Multivariate Bayesian Predictive Synthesis in Macroeconomic Forecasting. *Journal of the American Statistical Association* 115(531), 1092–1110.

McAlinn, K. and M. West (2019, May). Dynamic Bayesian predictive synthesis in time series forecasting. *Journal of Econometrics* 210(1), 155–169.

Nobre, A. A., A. M. Schmidt, and H. F. Lopes (2005, May). Spatio-temporal models for mapping the incidence of malaria in Pará. *Environmetrics* 16(3), 291–304.

Pan, S., L. Zhang, J. R. Bradley, and S. Banerjee (2025, May). Bayesian Inference for Spatial-Temporal Non-Gaussian Data Using Predictive Stacking. arXiv:2406.04655 [stat].

Paul-Christian Bürkner, J. G. and A. Vehtari (2020). Approximate leave-future-out cross-validation for Bayesian time series models. *Journal of Statistical Computation and Simulation* 90(14), 2499–2523.

Pherwani, P., N. Hass, and A. Yanchenko (2024). Spatiotemporal Modeling and Forecasting at Scale with Dynamic Generalized Linear Models. In *Proceedings of the 1st ACM SIGSPATIAL International Workshop on Geospatial Anomaly Detection*, GeoAnomalies '24, New York, NY, USA, pp. 16–27. Association for Computing Machinery. event-place: Atlanta, GA, USA.

Prado, R., M. Ferreira, and M. West (2021). *Time Series: Modeling, Computation, and Inference, Second Edition*. Chapman & Hall/CRC Texts in Statistical Science. CRC Press.

Presicce, L. and S. Banerjee (2024). Bayesian Transfer Learning for Artificially Intelligent Geospatial Systems: A Predictive Stacking Approach. *arXiv preprint*. arXiv:2410.09504 [stat.ME].

Quintana, J. M. and M. West (1987). An Analysis of International Exchange Rates Using Multivariate DLM's. *Journal of the Royal Statistical Society. Series D (The Statistician)* 36(2/3), 275–281.

Radev, S. T., U. K. Mertens, A. Voss, L. Ardizzone, and U. Köthe (2020). BayesFlow: Learning complex stochastic models with invertible neural networks. *IEEE transactions on neural networks and learning systems* 33(4), 1452–1466.

Ruiz Maraggi, L. M., L. W. Lake, and M. P. Walsh (2021, July). Using Bayesian Leave-One-Out and Leave-Future-Out Cross-Validation to Evaluate the Performance of Rate-Time Models to Forecast Production of Tight-Oil Wells. In *Proceedings of the 9th Unconventional Resources Technology Conference*, Volume Day 2 Tue, July 27, 2021 of *SPE/AAPG/SEG Unconventional Resources Technology Conference*, pp. D021S027R003.

Sainsbury-Dale, M., A. Zammit-Mangion, J. Richards, and R. Huser (2024). Neural Bayes Estimators for Irregular Spatial Data using Graph Neural Networks. arXiv:2310.02600.

Sandefur, J. (1990). *Discrete Dynamical Systems: Theory and Applications*. Clarendon Press.

Schmidt, A. M. and H. F. Lopes (2019). Dynamic models. In *Handbook of Environmental and Ecological Statistics*, pp. 57–80. Chapman & Hall.

Stein, M. L. (1988). Asymptotically Efficient Prediction of a Random Field with a Misspecified Covariance Function. *The Annals of Statistics* 16(1), 55–63.

Stein, M. L. and M. S. Handcock (1989). Some asymptotic properties of kriging when the covariance function is misspecified. *Mathematical Geology* 21, 171–190.

Stroud, J. R., P. Müller, and B. Sansó (2001). Dynamic models for spatiotemporal data. *Journal of the Royal Statistical Society: Series B (Statistical Methodology)* 63(4), 673–689.

Tallman, E. and M. West (2023, October). Bayesian predictive decision synthesis. *Journal of the Royal Statistical Society Series B: Statistical Methodology* 86(2), 340–363.

Tang, W., L. Zhang, and S. Banerjee (2021). On identifiability and consistency of the nugget in Gaussian spatial process models. *Journal of the Royal Statistical Society: Series B (Statistical Methodology)* 83(5), 1044–1070.

Tramblay, Y., L. Neppel, and J. Carreau (2011, September). Brief communication "Climatic covariates for the frequency analysis of heavy rainfall in the Mediterranean region". *Natural Hazards and Earth System Sciences* 11(9), 2463–2468.

van Osnabrugge, B., R. Uijlenhoet, and A. Weerts (2019, March). Contribution of potential evaporation forecasts to 10-day streamflow forecast skill for the Rhine River. *Hydrology and Earth System Sciences* 23(3), 1453–1467.

Vehtari, A., A. Gelman, and J. Gabry (2017). Practical Bayesian model evaluation using leave-one-out cross-validation and WAIC. *Statistics and Computing* 27(5), 1413–1432.

Vehtari, A., T. Mononen, V. Tolvanen, T. Sivula, and O. Winther (2016). Bayesian Leave-One-Out Cross-Validation Approximations for Gaussian Latent Variable Models. *Journal of Machine Learning Research* 17(103), 1–38.

Werbos, P. (1990, October). Backpropagation through time: what it does and how to do it. *Proceedings of the IEEE* 78(10), 1550–1560.

West, M. and J. Harrison (1997, February). *Bayesian Forecasting and Dynamic Models (Springer Series in Statistics)*. Springer-Verlag.

Wikle, C. K. and M. B. Hooten (2010, November). A general science-based framework for dynamical spatio-temporal models. *TEST* 19(3), 417–451.

Wolpert, D. H. (1992). Stacked generalization. *Neural Networks* 5(2), 241–259.

Yao, Y., A. Vehtari, D. Simpson, and A. Gelman (2018). Using Stacking to Average Bayesian Predictive Distributions (with Discussion). *Bayesian Analysis* 13(3), 917–1007.

Zammit-Mangion, A., M. Sainsbury-Dale, and R. Huser (2024). Neural Methods for Amortised Inference.

Zammit-Mangion, A., M. Sainsbury-Dale, and R. Huser (2025, March). Neural Methods for Amor-tized Inference. *Annual Review of Statistics and Its Application* 12(Volume 12, 2025), 311–335.

Zammit-Mangion, A. and C. K. Wikle (2020, June). Deep integro-difference equation models for spatio-temporal forecasting. *Spatial Statistics* 37, 100408.

Zhang, H. (2004). Inconsistent estimation and asymptotically equal interpolations in model-based geostatistics. *Journal of the American Statistical Association* 99(465), 250–261.

Zhang, L. and S. Banerjee (2022). Spatial factor modeling: A Bayesian matrix-normal approach for misaligned data. *Biometrics* 78(2), 560–573.

Zhang, L., W. Tang, and S. Banerjee (2025). Bayesian geostatistics using predictive stacking. *Journal of the American Statistical Association (In press)*.

Supplemental material: Adaptive Markovian Spatiotemporal Transfer Learning in Multivariate Bayesian Modeling

Luca Presicce and Sudipto Banerjee

Organization of the supplemental material

Section [S1](#) provides additional results and theoretical derivations for dynamic Bayesian predictive stacking. In particular, Section [S1.1](#) presents the analytical derivation of the DYNBPS optimization problem in Equation [\(11\)](#) (Section [2.2](#)), while Section [S1.2](#) investigates the aggregated weighting strategies for DYNBPS introduced in Section [2.2](#). Section [S2](#) describes the complementary methods and algorithms presented in Section [3](#), and Section [S3](#) reports supplementary simulation results assessing the impact of the proposed weighting strategies. Section [S4](#) provides details on non-spatial and spatial exploratory data analysis related to the case study in Section [5](#). Finally, Section [S5](#) presents complementary graphics supporting the main manuscript.

S1 Theoretical derivations

S1.1 Dynamic Bayesian predictive stacking

As presented in ([Yao et al., 2018](#), Section 3.1), and summarized in Section [2](#), the Bayesian predictive stacking problem arose as

$$\min_{w \in \mathcal{S}_1^J} d \left(\sum_{j=1}^J w_j p(\cdot | \mathcal{D}_t, \mathcal{M}_j), p^*(\cdot | \mathcal{D}_t) \right) \quad \text{or} \quad \max_{w \in \mathcal{S}_1^J} S \left(\sum_{j=1}^J w_j p(\cdot | \mathcal{D}_t, \mathcal{M}_j), p^*(\cdot | \mathcal{D}_t) \right). \quad (\text{S1})$$

The empirical approximation to Equation [\(S1\)](#) proposed in the original manuscript of [Yao et al. \(2018\)](#) relies on replacing the full predictive evaluated at a new data point with its corresponding LEAVE-ONE-OUT predictive distribution. In doing so, they aim to approximate the expectation of the score through a leave-one-out cross-validation estimator, avoiding overly optimistic estimates.

Here, we define a renewed stacking problem ad hoc for dynamic contexts. This is specially made for these scenarios where time-dependence is relevant, and one-step-ahead predictive distribution is more informative than the usual predictive distribution, while LOO fails (Snijders, 1988; Paul-Christian Bükner and Vehtari, 2020). In this matter, the proper scoring rule must be assessed with respect to the true one-step-ahead predictive distribution at a generic time instant τ , i.e. $p^*(Y_\tau | \mathcal{D}_{\tau-1})$. Defining the “dynamic” stacking problem as

$$\min_{w^{(\tau)} \in \mathcal{S}_1^J} d \left(\sum_{j=1}^J w_j^{(\tau)} p(\cdot | \mathcal{D}_{\tau-1}, \mathcal{M}_j), p^*(\cdot | \mathcal{D}_{\tau-1}) \right) \quad \text{or} \quad \max_{w^{(\tau)} \in \mathcal{S}_1^J} S \left(\sum_{j=1}^J w_j^{(\tau)} p(\cdot | \mathcal{D}_{\tau-1}, \mathcal{M}_j), p^*(\cdot | \mathcal{D}_{\tau-1}) \right). \quad (\text{S2})$$

Since it is again unknown, an approximation is required. In this situation, LOOCV does not provide an accurate approximation, as it does not account for the time ordering naturally present in time series data (Snijders, 1988). Conversely, LFO arises in the literature to solve precisely this issue. We then pursue an approximation to the expectation of the proper scoring rule. Indeed, proper scoring rules for two probabilistic forecasts can also be written as expectation (Gneiting and Raftery, 2007; Yao et al., 2018, for further details).

$$S \left(\sum_{j=1}^J w_j^{(\tau)} p(\cdot | \mathcal{D}_{\tau-1}, \mathcal{M}_j), p^*(\cdot | \mathcal{D}_{\tau-1}) \right) = \mathbb{E}_{p^*} \left[S \left(\sum_{j=1}^J w_j^{(\tau)} p(Y_\tau | \mathcal{D}_{\tau-1}, \mathcal{M}_j), Y_\tau \right) \right]. \quad (\text{S3})$$

Implementing the leave-future-out cross-validation, we derive the subsequent approximation to the expectation in (S3), which takes into account temporal dynamics

$$(\hat{w}_1^{(\tau)}, \dots, \hat{w}_J^{(\tau)})^\top = \arg \max_{w^{(\tau)} \in \mathcal{S}_1^J} \frac{1}{\tau-1} \sum_{t=1}^{\tau-1} S \left(\sum_{j=1}^J w_j^{(\tau)} p(Y_{t+1} | \mathcal{D}_t, \mathcal{M}_j), Y_{t+1} \right). \quad (\text{S4})$$

When using the logarithm score, they refer to it as the stacking of predictive distributions. We opt for the logarithm score since solving (11) again minimizes the Kullback-Leibler divergence from the true predictive distribution. In addition, it can be easily executed using convex optimization (Grant, 2005; Grant and Boyd, 2008). This leads to the optimization problem reported in Equation (11). Similarly, we refer to it as dynamic stacking of predictive distributions.

S1.2 Properties of aggregated dynamic Bayesian predictive weights

Let $W^{(\tau)} = \{\hat{w}_{i,j}^{(\tau)}\} \in [0, 1]^{n \times J}$ be a row-stochastic matrix, where each row sums to one, i.e.,

$$\sum_{j=1}^J w_{i,j} = 1, \quad \forall i = 1, \dots, n$$

This matrix is defined by collecting the individual-wise dynamic Bayesian predictive stacking weights computed using Equation (S2). Without loss of generality, we consider a generic time point $\tau \in \mathcal{T}$, but the same arguments are valid for each element of \mathcal{T} . Each row corresponds to a spatial observation, and the entries $\hat{w}_{i,j}^{(\tau)}$ are the DYNBPS weights assigned to the J model configurations \mathcal{M}_j , with $j = 1, \dots, J$. These entries represent a probability distribution over J candidate models for that observation.

To obtain a single distribution over the models, i.e., a weights vector, valid for all the observations, we consider two aggregation strategies: (i) global weights and (ii) consensus weights, as presented in Section 2.2. Both are shown here to yield valid probability vectors, thereby preserving the probabilistic interpretation of the original individual-wise weights.

The global weight vector $\hat{w}_G = \{\hat{w}_{G,j}\} \in \mathbb{R}^J$ is defined as the column-wise average of W , such that

$$\hat{w}_{G,j}^{(\tau)} = \frac{1}{n} \sum_{i=1}^n \hat{w}_{i,j}^{(\tau)}, \quad j = 1, \dots, J.$$

Proposition 1. $\hat{w}_G^{(\tau)}$ is a probability vector: $\hat{w}_{G,j}^{(\tau)} \in [0, 1]$ for all $j = 1, \dots, J$ and $\sum_{j=1}^J \hat{w}_{G,j}^{(\tau)} = 1$.

Proof. Since each element of $W^{(\tau)}$, $\hat{w}_{i,j}^{(\tau)} \in [0, 1]$, is clearly due to properties of the arithmetic mean that $0 \leq \hat{w}_{G,j}^{(\tau)} \leq 1$ for all j . Moreover,

$$\sum_{j=1}^J \hat{w}_{G,j}^{(\tau)} = \sum_{j=1}^J \frac{1}{n} \sum_{i=1}^n \hat{w}_{i,j}^{(\tau)} = \frac{1}{n} \sum_{i=1}^n \underbrace{\sum_{j=1}^J \hat{w}_{i,j}^{(\tau)}}_{=1} = \frac{1}{n} \cdot n = 1.$$

□

Thus, “global” averaging preserves the stochastic property, producing a blended global set of weights.

The consensus weight vector $\hat{w}_C^{(\tau)} = \{\hat{w}_{C,1}, \dots, \hat{w}_{C,J}\} \in \mathbb{R}^J$ is obtained by first identifying, for each observation i , the model index with the largest weight (i.e., the “preferred” model for that observation), and then normalizing the counts of such preferences.

Formally, let $j_i^{(\tau)} = \arg \max_{1 \leq j \leq J} \hat{w}_{i,j}^{(\tau)}$, with a deterministic tie-breaking rule (e.g., the smallest index). Define the count for model j as $c_j^{(\tau)} = |\{i : j_i^{(\tau)} = j\}|$, and set

$$\hat{w}_{C,j}^{(\tau)} = \frac{c_j^{(\tau)}}{n}, \quad j = 1, \dots, J.$$

Proposition 2. $\hat{w}_C^{(\tau)}$ is a probability vector: $\hat{w}_{C,j}^{(\tau)} \in [0, 1]$ for all j and $\sum_{j=1}^J \hat{w}_{C,j}^{(\tau)} = 1$.

Proof. Each observation contributes to exactly one count, so $\sum_{j=1}^J c_j = n$. Hence $0 \leq \hat{w}_{C,j}^{(\tau)} = \frac{c_j}{n} \leq 1$ and

$$\sum_{j=1}^J \hat{w}_{C,j}^{(\tau)} = \frac{1}{n} \sum_{j=1}^J c_j = \frac{n}{n} = 1.$$

□

This method yields a global distribution that reflects the plurality of observation-level preferences.

Both aggregation schemes therefore guarantee that the resulting vector is a proper probability distribution over the J models, making either suitable for subsequent use as weights in ensemble or decision-theoretic applications. The choice between them depends on whether a smooth blending of all weights or a majority-rule consensus is preferred.

S2 Computational details and algorithms

This Section collects and complements the algorithmic details underlying the predictive procedures discussed in Section 3. In particular, Algorithms S1 and S2 formalize the implementation of dynamic Bayesian predictive stacking for temporal forecasting and spatial interpolation, respectively.

The former describes a recursive procedure for generating one-step and multi-step-ahead posterior predictive samples for temporal forecasting using spatiotemporal models in Equation (8), by sequentially propagating uncertainty through time. The latter outlines the mechanism for spatial

Algorithm S1 DYNBPS - temporal forecasting

Require: Forecast horizon K , stacking weights $\{\hat{w}^{(t)}\}_{t=1}^T$, filtering parameters and inputs from Algorithm 2

Ensure: R posterior predictive samples from $\hat{p}(\Theta_{T+k}, Y_{T+k} | \mathcal{D}_T)$ for $k = 1, \dots, K$

1: **function:** DYNBPS-FORECAST $\left(\{\hat{w}^{(t)}, \{m_t^{(j)}, C_t^{(j)}, \Psi_t^{(j)}, \nu_t^{(j)}, \alpha^{(j)}, \phi^{(j)}\}_{j=1}^J\}_{t=0}^T, R, K\right)$

2: **for** $r = 1, \dots, R$ **do**

3: *# Draw model \mathcal{M}_j such that $j \sim \text{Multinom}(1, J, \{\hat{w}_1^{(T)}, \dots, \hat{w}_J^{(T)}\})$*

4: *# Compute joint posterior predictive parameters*

5: $A(0) \leftarrow m_T^{(j)}, R(0) \leftarrow C_T^{(j)}$

6: **for** $k = 1, \dots, K$ **do**

7: *# Compute observation and state row-covariance matrices*

8: $V_{T+k}^{(j)} \leftarrow \left(\frac{1-\alpha^{(j)}}{\alpha^{(j)}}\right) \mathbb{I}_n, W_{T+k}^{(j)} \leftarrow \begin{bmatrix} \mathbb{I}_p & 0_{p \times n} \\ 0_{n \times p} & \mathcal{R}_{T+k}(\mathcal{S}, \mathcal{S}; \phi^{(j)}) \end{bmatrix}$

9: *# Compute posterior predictive parameters*

10: $A_T(k) \leftarrow G_{T+k} A_T(k-1), q_T(k) \leftarrow F_{T+k} A_T(k)$

11: $R_T(k) \leftarrow G_{T+k} R_T(k-1) G_{T+k}^T + W_{T+k}, Q_T(k) \leftarrow F_{T+k} R_T(k) F_{T+k}^T + V_{T+k}$

12: *# Define joint posterior predictive parameters*

13: $A^*(k) \leftarrow \begin{bmatrix} A_T(k) \\ q_T(k) \end{bmatrix}, R^*(k) \leftarrow \begin{bmatrix} R_T(k) & F_{T+k} R_T(k) \\ R_T(k) F_{T+k}^T & Q_T(k) \end{bmatrix}$

14: *# Draw $\{\Theta_{T+k}^{(r)}, Y_{T+k}^{(r)}\}$ from $\text{T}_{p+n+n, q}(\nu_T^{(j)}, A^*(k), R^*(k), \Psi_T^{(j)})$*

15: *# Store $\{A^*(k), R^*(k)\}$ for the next iteration*

16: **end for**

17: **end for**

18: **return** R posterior predictive samples of $\{\Theta_{T+k}, Y_{T+k}\}$ for any $k = 1, \dots, K$

19: **end function**

Algorithm S2 DYNBPS - spatial prediction at time t

Require: Stacking weights $\hat{w}^{(t)}$, unobserved locations \mathcal{U} and their design matrix \tilde{X}_t , filtering parameters and inputs from Algorithm 2

Ensure: R posterior predictive samples from $\hat{p}(\tilde{Y}_t, \tilde{\Omega}_t | \mathcal{D}_t)$

1: **function:** DYNBPS-SPATPREDICT $\left(\hat{w}^{(t)}, \{m_t^{(j)}, C_t^{(j)}, \Psi_t^{(j)}, \nu_t^{(j)}, \alpha^{(j)}, \phi^{(j)}\}_{j=1}^J, R\right)$

2: **for** $r = 1, \dots, R$ **do**

3: *# Draw model \mathcal{M}_j such that $j \sim \text{Multinom}(1, J, \{\hat{w}_1^{(t)}, \dots, \hat{w}_J^{(t)}\})$*

4: *# Compute observation row-covariance matrix for new locations*

5: $\tilde{V}_t(\alpha) \leftarrow \left(\frac{1-\alpha}{\alpha}\right) \mathbb{I}_m$

6: *# Compute Shur complement parameters*

7: $\tilde{M}_t \leftarrow \mathcal{R}_t(\mathcal{U}, \mathcal{S}; \phi) \mathcal{R}_t^{-1}(\mathcal{S}, \mathcal{S}; \phi), \tilde{W}_t(\phi) \leftarrow \mathcal{R}_t(\mathcal{U}, \mathcal{U}; \phi) - \tilde{M}_t \mathcal{R}_t(\mathcal{S}, \mathcal{U}; \phi)$

8: *# Compute joint posterior predictive parameters*

9: $\chi_t \leftarrow \begin{bmatrix} \tilde{X}_t & \tilde{M}_t \\ 0 & \tilde{M}_t \end{bmatrix}, N_t \leftarrow \begin{bmatrix} \tilde{V}_t(\alpha) + \tilde{W}_t(\phi) & \tilde{W}_t(\phi) \\ \tilde{W}_t(\phi) & \tilde{W}_t(\phi) \end{bmatrix}$

10: $\mu_t \leftarrow \chi_t m_t, E_t \leftarrow \chi_t C_t \chi_t^T + N_t$

11: *# Draw $\{\tilde{Y}_t^{(r)}, \tilde{\Omega}_t^{(r)}\}$ from $\text{T}_{2m, q}(\nu_t^{(j)}, \mu_t, E_t, \Psi_t^{(j)})$*

12: **end for**

13: **return** R posterior predictive samples of $\{\tilde{Y}_t, \tilde{\Omega}_t\}$

14: **end function**

interpolation at a generic time point t , whereby posterior predictive samples of the multivariate latent spatial process and responses are drawn at unobserved locations using the results presented in Equation (10). Together with the methods presented in Section 3, these procedures are implemented

in the `spFFBSR` package to provide a framework for spatiotemporal modeling with uncertainty quantification via DYNBPS.

S3 Additional simulation experiment

S3.1 Space-time weights dynamics

In this simulation experiment, we investigated the different behaviors of Dynamic Bayesian predictive stacking weights. In Section 2.2, we introduce the concept of “global” weights (G) and “consensus” weights (C). This stems from the need to concentrate local information on weights, which dynbps actually provides (see Section 2.2 for motivation and further technical details). Both global and consensus weight sets work as central tendency extrapolations from their spatial distributions, allowing FFBS algorithm implementation, as detailed in Section 3. In particular, they reflect information on the average weight and the “consensus” among locations for each of the J candidate models at any time point. Although they mainly serve to retain computational admissibility, there are many interesting features we can obtain by investigating local weights and their dynamics across time. Thus, we report here a simulation experiment that provides more insight into these matters, allowing us to obtain model preferences “locally”.

We start our simulation experiment by generating a set of spatiotemporal synthetic data. We mainly follow the same simulation framework used in Section 4.2, without replications, as we focus on the clustering of weights. Then, we have values on $n \times q \times t$ outcome Y generated from (8) with $n = 500$, $q = 3$, $t = 100$ and $p = 2$, X includes two predictors generated from a standard uniform distribution over $[0, 1]$. While the $n \times n$ spatial correlation matrix V is specified using an exponential correlation function with $\phi = 4$ and $\alpha = 0.8$. See Section 4.2 for further details.

We start our discussion with the examination of Figure S1. We report here two panels, from left to right: “consensus” weights ($\hat{w}_C^{(t)}$) and “global” weights ($\hat{w}_G^{(t)}$) dynamics over time-points. Firstly, worth highlighting that, by construction of dynamic BPS, as the time instant grows, more information is available to determine the weights. This leads to the possible interpretation of the panels in Figure S1 as trace plots, i.e., reflecting the convergence of weights. That said, we notice a decreasing

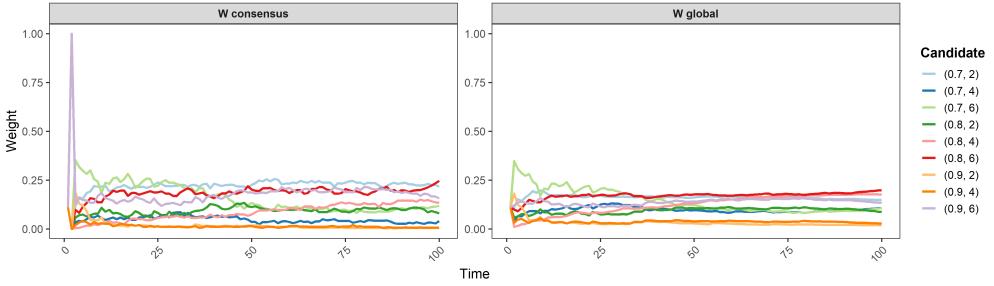


Figure S1: DYNBPS weights dynamics comparison over time: consensus weights (left panel), global weights (right panel)

variability in the magnitude of weights as time passes. Both approaches completely stabilize the weights' central tendency after about 30 time-points, even if $\hat{w}_G^{(t)}$ appears to have smoother and faster transitions. Moreover, we also noticed a greater separation in magnitude for $\hat{w}_C^{(t)}$, while spatially averaged weights ($\hat{w}_G^{(t)}$) tend to concentrate. Figure S1 also shows a model-ranking coherence between the two approaches, which means they give the same predictive “relevance” to the same model. Therefore, we can state that there are no significant differences between using one method or the other, as we obtain comparable results.

Hereafter, we will consider global weights $\hat{w}_G^{(t)}$. Figure S2 represents the empirical estimates for $\{\alpha, \phi\}$ at different time points. As shown in Figure S1, we could interpret these as trace plots. Let us note that the estimates are given as follows: $\hat{\alpha}_t = \sum_{j=1}^J \hat{w}_G^{(t)} \alpha_j$ and $\hat{\phi}_t = \sum_{j=1}^J \hat{w}_G^{(t)} \phi_j$. In Figure S2, the left-most panel shows the trace plot for α , while the rightmost panel shows the trace plot for ϕ . Both are, in some sense, attracted to the true values (dashed lines), but for α , there is an underestimation, in contrast to ϕ , which is overestimated. The latter, which can be identified as “oversmoothing” is typical when working with a distributed learning approach (see e.g., [Guhaniyogi and Banerjee, 2018](#); [Presicce and Banerjee, 2024](#)). The underestimation for α may actually stem from the oversmoothing of ϕ . Indeed, the model could underestimate the proportion of spatial variance, i.e., α , when a larger ϕ is preferred, as it suggests a stronger spatial dependence, which, ceteris paribus, should absorb less variability from the “total,” while still retaining the same spatial dependence. The investigation into the model balancing behavior of the dynamic stacking weights remains of interest, but we will reserve it for future work. At the moment, we can only conclude that there is a good attitude of the DYNBPS, at least when working in a \mathcal{M} -closed setting, as the experiment was.

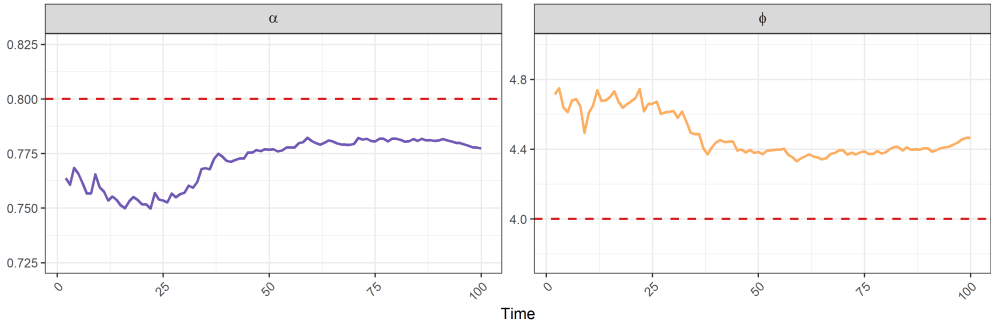


Figure S2: Parameter estimates dynamics against true value (red dashed line) over time: α point-estimates (left panel), ϕ point-estimates (right panel)

Lastly, we extrapolate insights from location-wise weights, which are shown in Figure S3. This panel is twofold: the average weight of models and the spatial distribution of weights colored per model. The latter makes use of the Voronoi tessellation to aid interpretation. To better understand the leftmost subplot in Figure S3, consider each colored bar as the frequency of locations that “prefer” that model. Where preference is expressed as the greatest weight. The same reasoning applies to the right subplot: it shows for each location which model received the greatest weight, i.e., the preferred model. Figure S3 clearly indicates that most locations prefer model $\{\alpha = 0.8, \phi = 6\}$, but the second preferred model is the true one, i.e., $\{\alpha = 0.8, \phi = 4\}$. However, many locations do not prefer the true model, as in the data-generating process, the conjunction between spatial variability and non-spatial associations among variables leads to sample georeferenced points with individual characteristics, for which the posterior predictive distribution pushes towards different values. We actually average out locally dependent micro-characteristics, as justified by the backward sampling, which aims to identify a common set of parameters. However, the methodological contribution allows for further investigation of many other perspectives, giving users a flexible level of interpretability for the analysis. From Figure S3, we can conclude that every location has a personal set of weights based on the local evaluation of posterior predictive distributions. Even though it may be computationally cumbersome to start a local analysis for all the points, there is still the opportunity to individually investigate each point, which corresponds to a multivariate time series by itself. This implies that from the joint procedure, you can also choose to study a subset of points that may be of interest for a specific research question. Once forward filtering with weights is complete, backward sampling

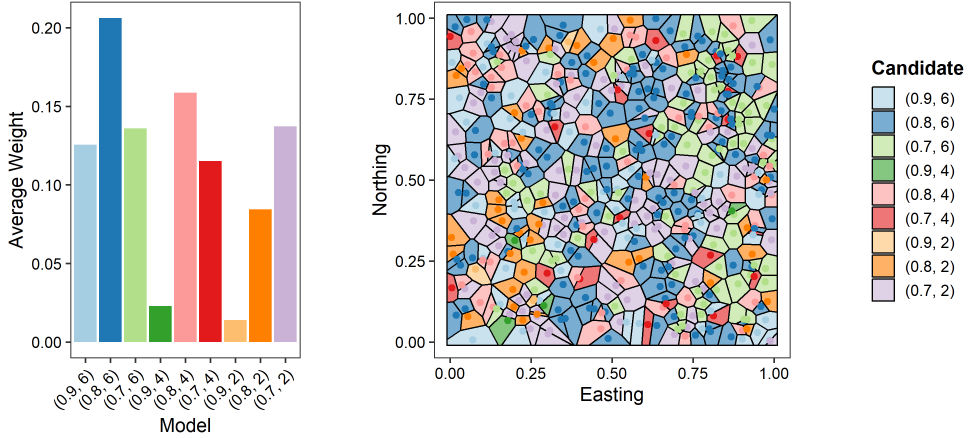


Figure S3: Location-wise weights spatial preference for each competitive model: bar plot of preference proportion (left panel), location-wise preferred model over Voronoi tassellation

Table S1: Summary statistics and visual representation of response variables.

Variable	Mean	Std.Dev	Min.	Max.	Histogram	Boxplot
Monthly temperature	13.043	8.444	-17.059	35.032		
Monthly precipitation	1.787	1.082	0.002	7.163		
Monthly wind speed	4.541	1.685	1.795	12.067		
Monthly evaporation	1.858	1.165	0.030	6.384		

can be performed for the point of interest using an individual set of weights that reflects local model preferences.

S4 Exploratory data analysis

Our current investigation utilizes high-resolution climate data from the Copernicus Climate Change Service (C3S) Atlas, a multi-source dataset developed within the European Union’s Copernicus Programme. The C3S Atlas compiles harmonized climate variables from different sources, including satellite remote-sensing and in-situ monitoring networks. These datasets are accessible through the Climate Data Store (CDS) and conform to the ACDD “Netcdf4metadata” conventions, ensuring compatibility, reproducibility across climate data analysis, and consistency for long-term climate monitoring.

Table S1 presents summary statistics for the four climate variables, together with histograms and boxplots for their distributions, without considering their spatiotemporal structure.

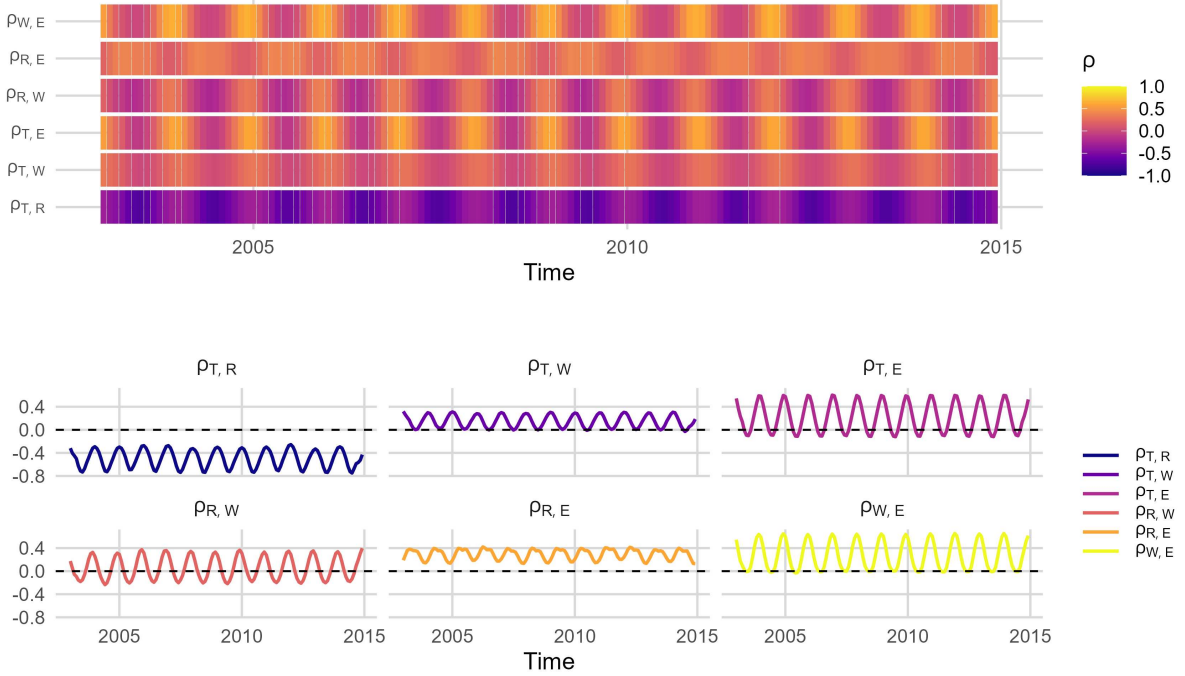


Figure S4: Correlation analysis between response variables over time: heatmap of correlation matrix elements (top panel), and time series of correlation matrix elements (bottom panel). Where T = monthly temperature, R = monthly precipitation/rain, W = monthly wind speed, E = monthly evaporation

We investigate inter-variable temporal dependence by analyzing the evolution of pairwise correlations over time. Figure S4 presents two complementary views: a heatmap showing the elements of the correlation matrix at each month and a time series of individual correlation coefficients. These diagnostics indicate pronounced seasonal modulation in all variable pairs, with coherent but magnitude-varying cycles driven by the underlying atmospheric processes.

We compute empirical spatiotemporal variograms on residuals to quantify the joint spatial and temporal dependence for each climate variable. Due to the strong seasonal effects, the residuals were obtained by regressing each variable in Y on relevant predictors and monthly seasonal dummy variables, see Section 5. We estimated the empirical spatiotemporal variograms using the `gstat` and `spacetime` in R.

A separable parametric model was fitted for each variable. This model was chosen for its interpretability and computational efficiency, as it assumes that spatial and temporal dependence can be modeled independently while still capturing the main features of the covariance structure. We combined an exponential spatial component with nugget 0.1, partial sill 1, and range 10; and an

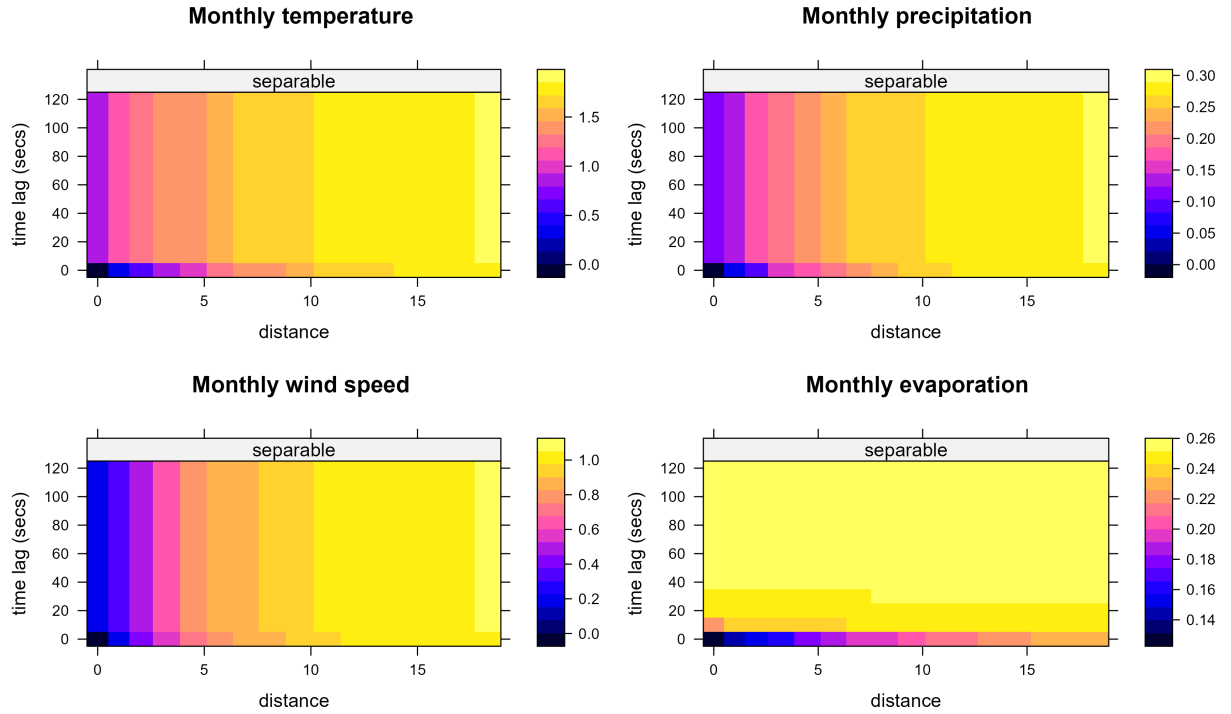


Figure S5: Spatiotemporal sample variogram computed on residuals: one panel for each response variable

exponential temporal component with nugget 0.1, partial sill 1, and range 5 months. The variograms were computed over all the training temporal lags, from 0 to 120, with a 10-month increment.

Figure S5 presents the fitted spatiotemporal variogram for all four response variables. The variogram analysis reveals a clear dichotomy. Atmospheric variables, like temperature, precipitation, and wind speed, all exhibit strong and persistent temporal memory, with autocorrelation lasting for long periods; wind speed shows the most robust temporal structure.

Spatially, their patterns are more localized, with wind speed again being more scattered. In contrast, evaporation behaves uniquely with respect to the other outcomes: it has a very short temporal memory, becoming uncorrelated fairly quickly, while its spatial pattern is the most extensive but also the one characterized by more noise; resulting dominated by fine-scale variations.

The fitted parameters supported the graphical interpretations, while we made use of them as starting points, composing the grid of values for α , and ϕ needed to implement DYNBPS. For further details, see Section 5.

To visualize large-scale spatiotemporal patterns, we constructed two Hovmöller diagrams, comparing the time evolution with respect to latitude and longitude, respectively.

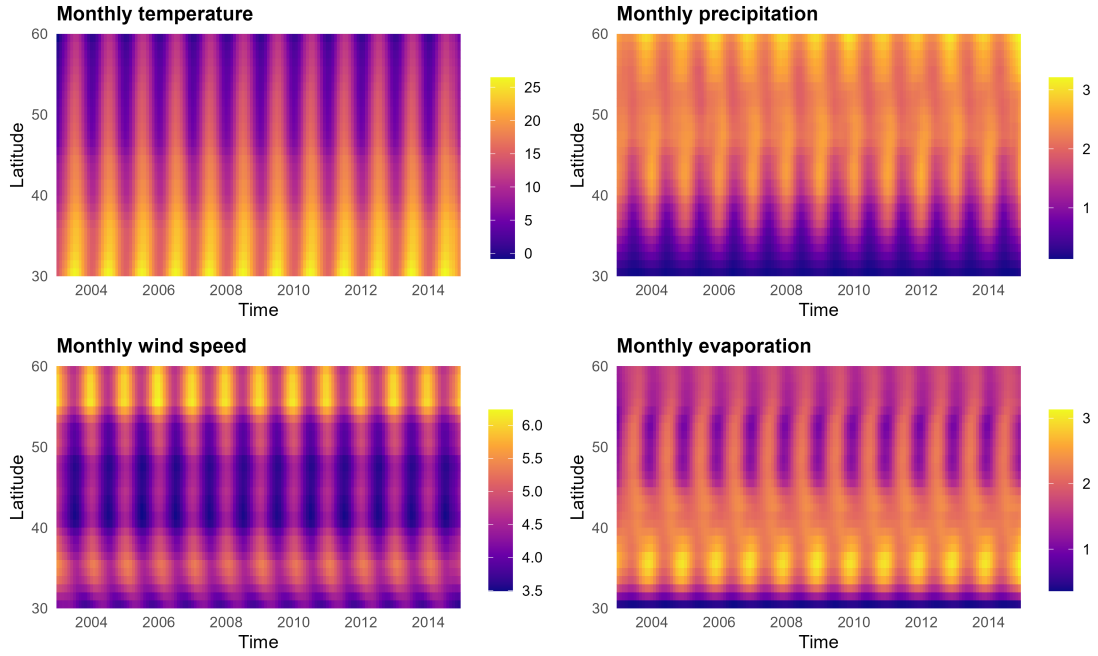


Figure S6: Hövmoller diagram by latitude for spatiotemporal atmospheric outcomes: : time (x-axis) against latitude (y-axis)

Figure S6 shows the Latitude-wise diagram, where for each month, the variable averages were computed along longitudes to display the northward propagation of atmospheric variables. Seasonal variability is clearly observed, highlighting strong and almost-linear latitudinal gradients in temperature and precipitation, while still showing smoothed but complex gradients for wind speed and evaporation. Unexpectedly, lower latitudes correspond to high temperature and low precipitation, inverting the tendency going northward. Despite the strong seasonality, worth to be noticed a clear stationarity for all the considered period, which can be seen for all the outcomes.

Conversely, in Figure S7 we present Hövmoller diagrams with respect to longitude, where variable averages were computed along latitudes to illustrate the eastward propagating structures, capturing zonal patterns such as recurring shifts in precipitation and wind dynamics across the study region. However, seems to have less variability along longitudes as presenting smoother surfaces for all variables, but evaporation still presents a complex structure. Strong seasonality and stationarity remain in longitude.

Together, the residual-based spatiotemporal variograms and Hovmöller diagrams provide strong evidence of structured dependencies across both space and time, as well as the presence of strong seasonality and stationarity in propagating structure. These diagnostics confirm that a multivariate spatiotemporal modeling framework is appropriate for capturing complex climate dynamics and

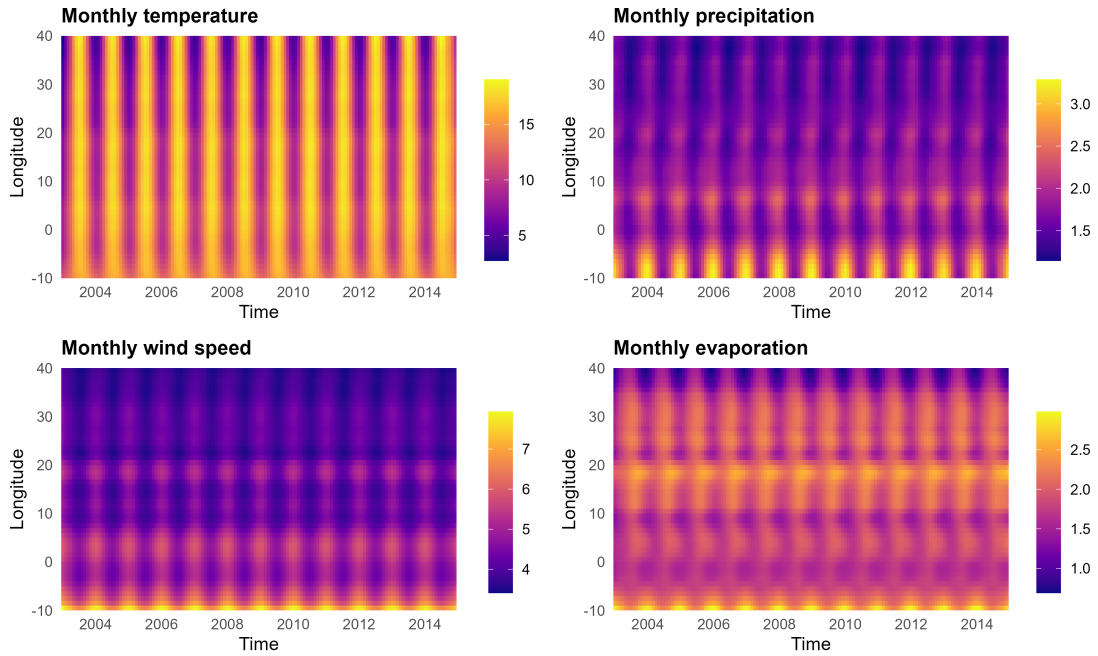


Figure S7: Hövmöller diagram by longitude for spatiotemporal atmospheric outcomes: time (x-axis) against longitude (y-axis)

justifies the predictive and inferential analyses presented in Section 5. Such an approach exploits the evolving cross-variable dependence and enables the borrowing of information across space and time.

S5 Additional figures

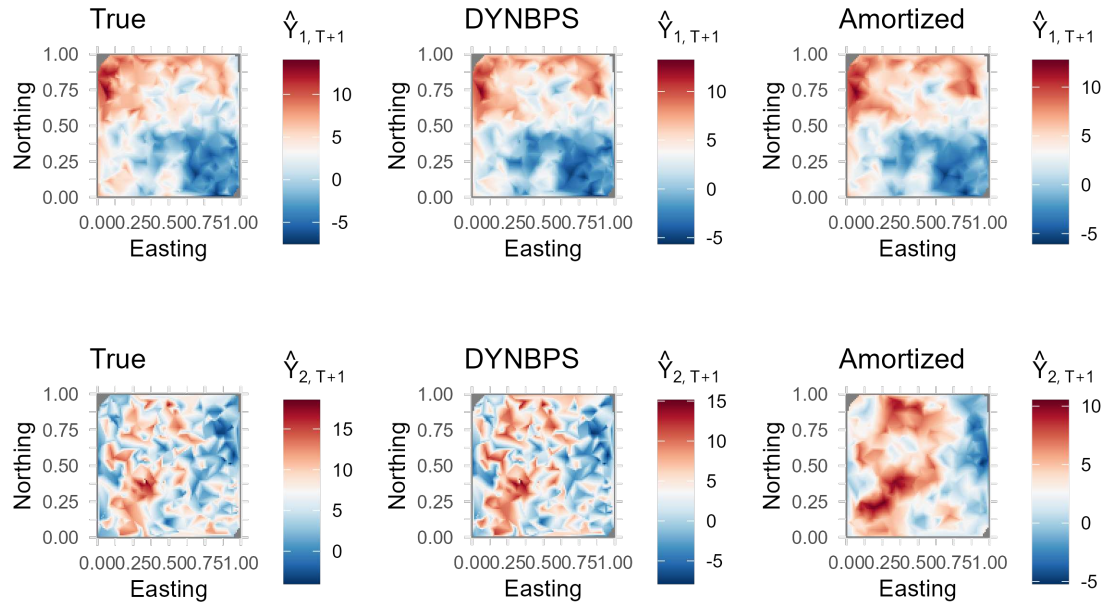


Figure S8: Spatial response Y one-step ahead forecast surface interpolations: true spatial process Ω (leftmost column), 50-th quantile DYNBPS forecast (center column), 50-th quantile amortized forecast (rightmost column); each row corresponds to an outcome

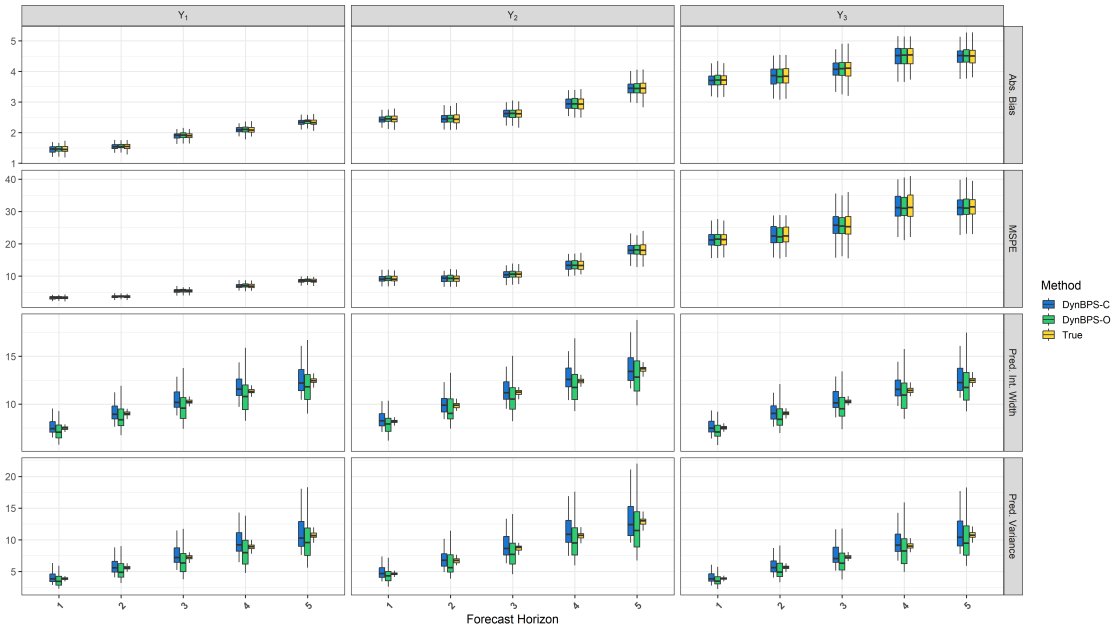


Figure S9: Predictive metrics for each response variable - over 50 replications

Figure S10: Predictive metrics at each time point for each component of the response matrix Y , under the considered model configurations and 50 replications: absolute bias (first row), mean squared prediction error (second row), predictive interval width (third row), predictive variance (fourth row)

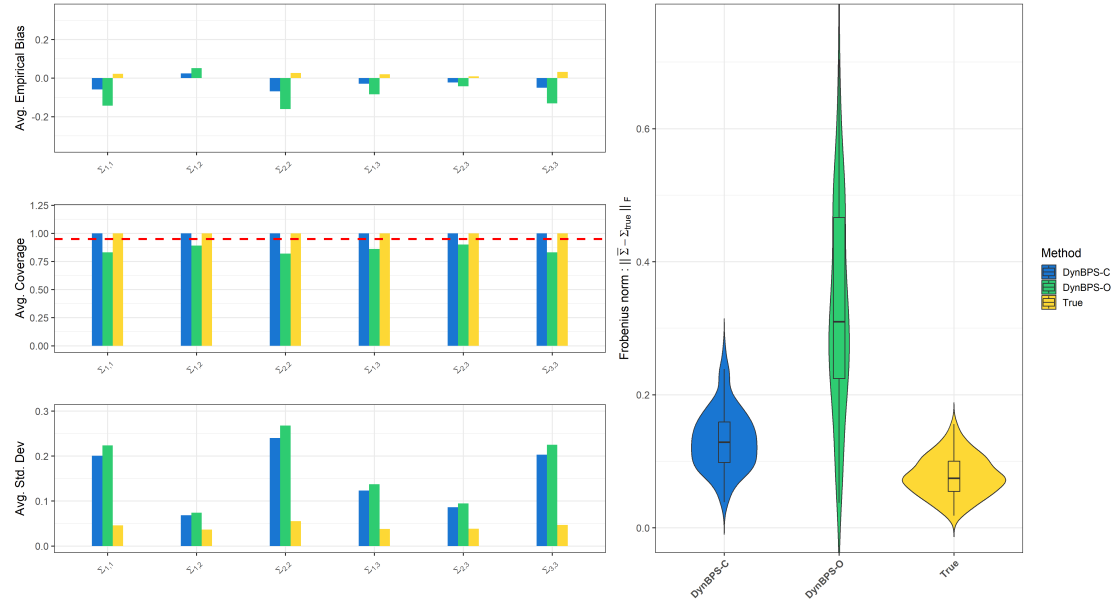


Figure S11: Posterior metrics at each time point for Σ , under the considered model configurations and 50 replications: average empirical bias (top left), average credible interval coverage (middle left), average posterior standard deviation (bottom left), Frobenius norm distribution (right)

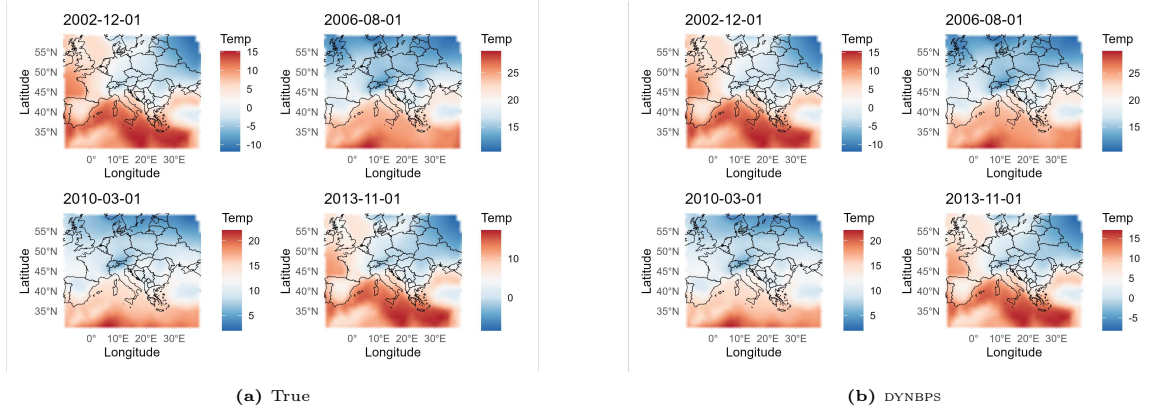


Figure S12: One-step ahead monthly temperature forecast at different time points

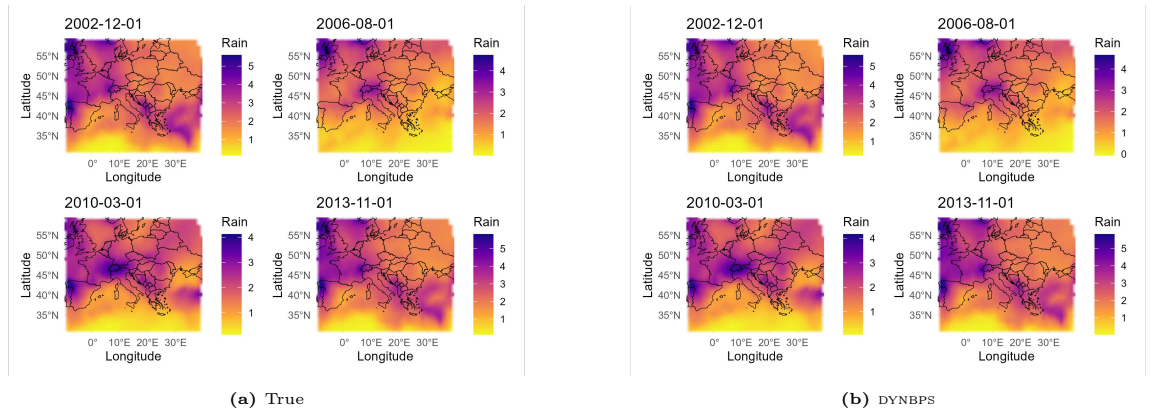


Figure S13: One-step ahead monthly precipitation forecast at different time points

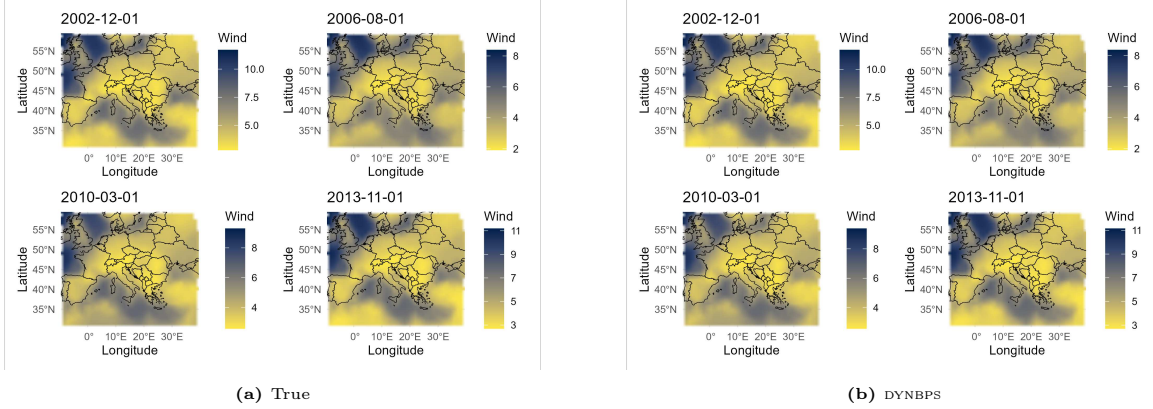


Figure S14: One-step ahead monthly wind speed forecast at different time points

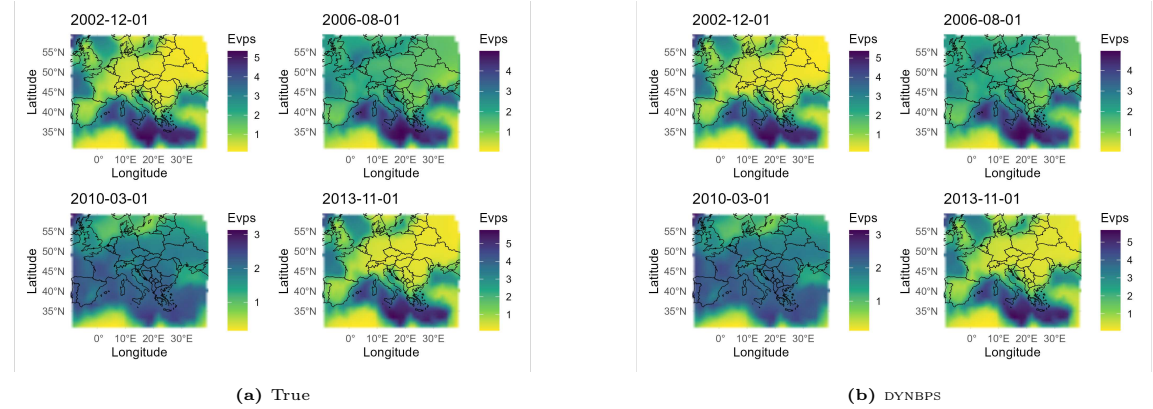


Figure S15: One-step ahead monthly evaporation forecast at different time points

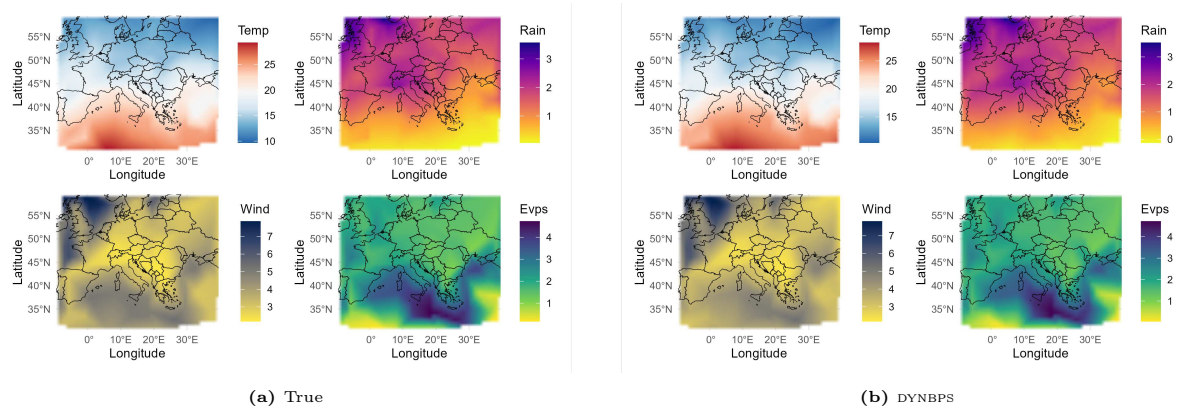


Figure S16: Spatial surface interpolation at unobserved time (in sample)

References

Gneiting, T. and A. E. Raftery (2007). Strictly Proper Scoring Rules, Prediction, and Estimation. *Journal of the American Statistical Association* 102(477), 359–378.

Grant, M. and S. Boyd (2008). Graph implementations for nonsmooth convex programs. In V. Blondel, S. Boyd, and H. Kimura (Eds.), *Recent Advances in Learning and Control*, Lecture Notes in Control and Information Sciences, pp. 95–110. Springer-Verlag Limited.

Grant, M. C. (2005). *Disciplined convex programming*. PhD Thesis, Stanford University.

Guhaniyogi, R. and S. Banerjee (2018). Meta-Kriging: Scalable Bayesian Modeling and Inference for Massive Spatial Datasets. *Technometrics* 60(4), 430–444.

Paul-Christian Bürkner, J. G. and A. Vehtari (2020). Approximate leave-future-out cross-validation for Bayesian time series models. *Journal of Statistical Computation and Simulation* 90(14), 2499–2523.

Presicce, L. and S. Banerjee (2024). Bayesian Transfer Learning for Artificially Intelligent Geospatial Systems: A Predictive Stacking Approach. *arXiv preprint*. arXiv:2410.09504 [stat.ME].

Snijders, T. A. B. (1988). On Cross-Validation for Predictor Evaluation in Time Series. In T. K. Dijkstra (Ed.), *On Model Uncertainty and its Statistical Implications*, Berlin, Heidelberg, pp. 56–69. Springer Berlin Heidelberg.

Yao, Y., A. Vehtari, D. Simpson, and A. Gelman (2018). Using Stacking to Average Bayesian Predictive Distributions (with Discussion). *Bayesian Analysis* 13(3), 917–1007.